Journal Pre-proof

Record of seismic slip in carbonates: insights from the Venere Fault during the 1915 Avezzano earthquake (Mw 7.0), Central Italy

Nina Zamani, Sara Satolli, Michael Murphy, Francois Demory, Bruno Pace, Jérôme Gattacceca, Ján Kaňuk, Michaela Nováková, Raphael Gottardi, Eric C. Ferré

PII: S0191-8141(25)00096-3

DOI: https://doi.org/10.1016/j.jsg.2025.105421

Reference: SG 105421

To appear in: *Journal of Structural Geology*

Received Date: 23 December 2024

Revised Date: 18 March 2025

Accepted Date: 25 March 2025

Please cite this article as: Zamani, N., Satolli, S., Murphy, M., Demory, F., Pace, B., Gattacceca, J., Kaňuk, J., Nováková, M., Gottardi, R., Ferré, E.C., Record of seismic slip in carbonates: insights from the Venere Fault during the 1915 Avezzano earthquake (Mw 7.0), Central Italy, *Journal of Structural Geology*, https://doi.org/10.1016/j.jsg.2025.105421.

Record of seismic slip in carbonates: insights from the Venere Fault during the 1915 Avezzano earthquake (Mw 7.0), Central Italy

Nina Zamani[1], Sara Satolli[2], Michael Murphy[1], Francois Demory[3], Bruno Pace[4], Jérôme Gattacceca[3], Ján Kaňuk[5], Michaela Nováková[6], Raphael Gottardi[7], and Eric C. Ferré[8]

[1] Department of Earth & Atmospheric Sciences, University of Houston, Houston, TX 77204, U.S.A.
[2] Engineering and Geology Department, Università degli Studi "G. d'Annunzio" di Chieti e Pescara, Chieti, Italy
[3] CNRS, Aix Marseille University, IRD, INRAE, CEREGE, Aix-en-Provence, France
[4] Department of Engineering and Geology, University "G. d'Annunzio" of Chieti-Pescara, Via Dei Vestini 31, 66100, Chieti, Italy
[5] PHOTOMAP, s.r.o., Poludníková 3/1453, 040 12 Košice, Slovakia
[6] Institute of Geography, Faculty of Science, Pavol Jozef Šafárik University in Košice, Jesenná 5, 040 01, Košice, Slovakia
[7] Department of Geosciences, Auburn University, Auburn, AL 36849, U.S.A.
[8] Department of Geological Sciences, New Mexico State University, NM, 88003, U.S.A.

Abstract

The Mw 7.0 Avezzano earthquake in the Abbruzzo region of Italy claimed ~33,000 lives on January 13, 1915 making it one of the worst disasters in modern Italian history. The main rupture occurred along the Venere Fault, characterized by a polished, locally shiny, or powdery fault mirror showing extensive downdip striations, slickensides, and local reddish iron-oxide/hydroxide stains. The layer immediately below the mirror is a carbonate ultracataclasite that locally grades into an unconsolidated carbonate gouge.

This type of carbonate fault mirror typically forms through two distinct synkinematic processes: i) intense frictional heating causing decarbonation, or ii) progressive grain-size reduction during slip at seismic velocities. In either case, friction drops substantially after initial displacement. The first process also results in intense fault pressurization followed by subsequent drastic drop in normal stress. Despite recent advances, the switch from high-friction/low slip velocity to low-friction/high slip velocity conditions in carbonate is still not fully understood.

The Venere Fault, characterized by proven friction at seismic slip velocity, provides an ideal setting to investigate the nature and extent of dynamic weakening processes in carbonate faults. We use the high temperature sensitivity of iron oxide/hydroxide assemblages, and their magnetic remanence, to estimate frictional heat. Evidence for seismic slip in iron oxides and temperature uniformity along the fault surface have been tested through demagnetization experiments and 1D heat conduction modeling. Our data shows that the fault mirror underwent frictional heating during the 0.8 m slip event, but that this displacement was insufficient to reach pervasive decarbonation. We constrain the peak coseismic temperature along the fault plane to <400ºC through demagnetization experiments and 1D heat conduction modeling. Our results emphasize that coseismic deformation along natural faults is complex and therefore requires complementary field observations at multiple scales in order to encompass a broad range of faulting processes.

Keywords: Avezzano earthquake, Venere Fault, carbonate deformation, frictional heating, seismic slip

Highlights:

- Carbonate fault mirrors form during seismic slip at certain velocities
- TLS data reveals fault mirror's roughness and asymmetric draping structure

- Frictional heating and decarbonation are not necessary for carbonate fault mirror development
- Magnetic fabric analysis (AARM) reveals that magnetite dominates as a seismic indicator
- Study shows decarbonation did not play a major role in the 1915 Avezzano earthquake

1. Introduction

As a major part of the world's seismicity occurs in carbonates in highly populated regions, it is increasingly crucial to understand *seismic rupture* in these rocks (Passelègue et al., 2019). In Italy, major earthquakes such as the 1915 M_w7.0 Avezzano, the 2009 M_w6.3 L'Aquila, and the 2016 M_w6.6 central Italy earthquakes respectively claimed the lives of ca. 33000, 308, and 289 people.

Friction experiments have significantly improved our understanding of the dynamic slip behavior of fault rocks under conditions simulating natural slow to fast earthquakes (0.1 to 10 m/s; Hirose and Shimamoto, 2005; Mizoguchi et al., 2007; Di Toro et al., 2010; 2011; Niemeijer et al., 2012; Passelègue et al., 2019; Chen et al., 2021). Such experiments on carbonates commonly reproduce the shiny surfaces formed on natural carbonate fault planes, *i.e.*, fault mirrors (Siman-Tov et al., 2013; Pozzi et al., 2018; Passelègue et al., 2019; Ohl et al., 2020).

However, these analog experiments have inherent limitations, including the need for relatively homogeneous materials, and small sample size (typically only a few centimeters). As a consequence, they cannot fully capture the complex lithological and geometrical variations present along natural fault planes. Conversely, field studies have consistently revealed new insights into seismogenic fault dynamics that cannot be easily accomplished through laboratory experiments due to scaling issues. In addition, results from drilling projects targeting seismogenic faults, *e.g.*, SAFOD, Chelungpu, Aigion, Wenchuan, Hikurangi, and the Alpine Fault (Lockner et al., 2011; Ma et al., 2006; Cornet et al., 2004; Li et al., 2013; Fagereng et al., 2019; Sutherland et al., 2012), further highlight the limitations of relying on one-dimensional outcrop data to infer large-scale slip behavior during rupture.

Investigations of carbonate-hosted seismogenic faults at the outcrop scale have provided critical insights into their slip behavior over geological time (*e.g.*, Rowe et al., 2012; Fondriest et al., 2015). Most seismogenic faults alternate between locked and creeping states, and understanding this behavior is vital for risk assessment (*e.g.*, Palyvos et al., 2005). Deformation experiments have successfully reproduced this stick-slip behavior (Bullock et al., 2014), they typically focus on asperities determined primarily by material grain size. In contrast, natural fault asperities are often much larger (Sagy and Broadsky, 2009), suggesting that laboratory experiments may not fully account for the complexities of seismic slip. Furthermore, experimental setups are limited by simplified geometries and homogeneous material compositions (Bedford et al., 2022). Therefore, further investigation of carbonate-hosted seismogenic faults is needed to elucidate faulting processes at smaller scales.

During large-magnitude seismic events, carbonate-hosted faults respond differently than those hosted by quartzo-feldspathic rocks (*e.g.*, Passelègue et al., 2019). The latter may undergo frictional melting and coseismic dynamic weakening (*e.g.*, Sibson, 1975; Hirose and Shimamoto, 2005; Sibson et al., 2006; Spray, 2010; Lavallée et al., 2015). In contrast, carbonate-hosted faults may undergo decarbonation, resulting from frictional heating above 400ºC (Han et al., 2007; 2010; Rowe et al., 2012; Kim et al., 2021), which significantly reduces normal stress due to CO_2 overpressure hence lubricating the fault surface (Sulem and Famin, 2009; Brantut et al., 2010; Kim et al., 2021; Gunatilake and Miller, 2022). Sudden lubrification may also lead to supershear conditions (Passelègue et al., 2019), thus resulting in increased ground shaking and peak ground velocities causing greater damage.

In the Abruzzo region, Italy, the extensive exposure, accessibility in the Santilli quarry and the extent of previous investigations makes the Venere Fault, an ideal natural example to compare to laboratory experiments (*e.g.*, Agosta and Aydin, 2006; Smith et al., 2011; Cella et al., 2021; Volatili et al., 2022; Sgobba and Pacor, 2023). Like many faults in Central Italy, the Venere Fault experienced catastrophic rupture (M_w7), notably causing tens of thousands of casualties in Avezzano in 1915 (Oddone, 1915; Serva et al., 1986; Moro et al., 2009). Although the average slip was relatively modest (~0.7 m), the resulting devastation highlights the need for a deeper understanding of such faults.

Here we investigate the magnetic fabrics of the seismic slip zone, *i.e.*, the fault mirror, in carbonate fault rocks to determine how coseismic deformation is recorded. Carbonates, being iron-poor, generally do not preserve deformation-related magnetic fabrics well (Borradaile and Jackson, 2004; Yang et al., 2020). At the Venere fault, the challenge consists in acquiring deformation-related magnetic fabrics on rocks made almost entirely of pure calcite (Merico et al., 2020, this study). We use the anisotropy of anhysteretic remanence magnetization (AARM) to evaluate if this method provides insights in paleoseismic deformation in fault carbonates. We also assess frictional heat using thermal demagnetization experiments.

2. Simplified geological setting

The central Apennine region underwent Neogene fold-and-thrust belt deformation followed by tectonic inversion marked by extension along numerous NW-SE trending listric normal faults resulting in formation of intermontane basins (*e.g.*, Carmignani and Kligfield, 1990; Cello et al., 1997; Vezzani et al., 2010; Tortorici et al., 2019; Curzi et al., 2021; Walker et al., 2021; Smeraglia et al., 2024), although the inversion history of these basins might be more complex (*e.g.*, Scisciani, 2009). Slab retreat and detachment constitute the main drivers of this inversion (*e.g.*, Fellin et al., 2022). The normal faults typically cut through lacustrine/fluvial deposits and produce prominent carbonate bedrock fault scarps. Most of these faults exhibit relatively modest slip rates (< 1 mm/yr) and show historic seismic activity (*e.g.*, Galadini and Messina, 1994; Cowie et al., 2017; Carafa et al., 2020). The largest intermontane basin of the Apennines, the Fucino Basin, developed primarily as a half graben along the Venere Fault on its Eastern flank. The Tre Monti Fault to the North of the basin defines its rhomb shape and shares many structural characteristics including bedrock type and timing of seismic deformation with the Venere Fault (Figure 1; Smith et al., 2011). The Venere Fault extends across the Fucino Basin from SE to NW and may be genetically connected to the L'Aquila-Celano fault system to the NW, thereby forming a >40 km-long fault network (Villani et al., 2015).

The Venere Fault, near the village of Gioia dei Marsi, is a 10 km-long, NW trending, SW dipping normal fault with a minor right-lateral strike-slip component (Piccardi et al., 1999; Cavinato et al., 2002; Agosta and Kirschner, 2001) and total rupture length of 38 km (Boncio et al., 2016). This fault extends ~10 km deep (Ghisetti and Vezzani, 1999) and juxtaposes Meso-Cenozoic platform carbonates in the footwall against the late Pliocene – late Pleistocene fluvio-lacustrine sediments of the Fucino Basin (Galadini and Messina, 1994). Focal mechanism solutions for the Mw 7.0 1915 earthquake suggest a broadly ENE oriented tension axis (Gasparini et al., 1985), while trench investigations document purely dip-slip extension (Michetti et al., 1996). A number of major seismic events have been identified along this fault during the following intervals 10800-5600 B.C., 6000-3600 B.C., 885-1349 A.D., and 550-885 A.D. (Michetti et al., 1996; Galadini and Galli, 1999). An average displacement rate is estimated to be 0.4–1.0 mm/yr, with down-dip slip toward N229º (Michetti et al., 1996; Piccardi et al., 1999). The Venere Fault (Figure 2) consists of multiple strands sharing similar strike N119º and 46º dip (Agosta and Aydin, 2006). The footwall, exposed along bedrock fault scarps, has been exhumed by ~ 0.6 to 1 km, indicating that the fault likely experienced a prolonged slip history (Agosta and Aydin, 2006; Figure 3 - this study). Figure 3E shows the fault macroscopic architecture which consists of the following structural domains: (1) undeformed rocks, (2) damage zone - gouge, (3) fault core - breccia and cataclasite, and (4) principal planar slip surface - fault mirror (fm). The fault architecture consists of a 100-m thick fault damage zone in the footwall showing increasing deformation intensity towards a <1 m-thick fault core (domains 3 and 4). Also, as suggested by previous isotope studies (Agosta and Kirschner, 2003), the structural domains of the Venere Fault are compartmentalized. The authors concluded that fluid infiltration, mostly of meteoric origin, is particularly detectable in fault mirror, whereas the fault core was impermeable.

In the Santilli quarry (Figure 3A), the Venere Fault presents a ~80 m long continuous Holocene bedrock fault scarp that was reactivated during the 1915 earthquake with a coseismic down-dip slip of ~0.8 m (Figure 3A, Serva et al., 1986; 2002; Ward and Valensise, 1989). The scarp dip angle ranges from ~30 to 70º, with an average of 46º and a consistent strike at ~N119º (Figure 3). A previously reported 2nd order fault (Volatili et al., 2022), located north of the main slip zone, is cut by several transverse faults that also bear normal dip-slip slickensides.

3. Methods

Terrestrial laser scanning (TLS) and unmanned aerial vehicle (UAV) surveys were conducted under stable weather conditions, with a nearly complete cloud cover that provided diffuse lighting, over a period of ~8 minutes. The TLS was performed using the FARO Focus 3D X130 terrestrial laser scanner, at resolution set to 1/4 of its maximum, with an angular scanning step of 0.036°, resulting in point spacing of ~6.28 mm. Twelve scanning positions ~10 m apart were established, ~6 to 8 m from the fault scarp, along with 8 ground control points measured using a GNSS device using the RTK method.

For the 3D photogrammetric model, a DJI Mavic 2 Pro UAV was used at a height of 40 m above ground level combined with oblique imagery (3 flight lines, 45º camera tilt, at a 25 m distance from the scarp) resulting in 680 images. The photogrammetric model was generated using Agisoft Metashape software. The orthophotomap was projected onto the plane best fitting the inclined fault wall.

The joint photogrammetric and TLS surveys were used to provide comprehensive and continuous structural information across the exposed fault plane (strike and dip) and for further calculations and interpretations. The point cloud was segmented, and non-fault features, such as grass or other artefacts large-scale grove marks made by excavator teeth, were removed. Dip and dip direction values were subsequently assigned to each point by converting the normal vectors in Cloud Compare software.

Polished petrographic thin-sections were observed with a Leica DM750P optical polarizing microscope attached to a digital camera and a Hitachi S-3400N II scanning electron microscope. X-ray diffraction analysis of powdered rocks was performed using a *Rigaku* Miniflex 600 benchtop compact diffractometer.

The magnetic measurements were performed at the CEREGE paleomagnetic laboratory. Thermal demagnetization of Natural Remanent Magnetization (NRM) and Isothermal Remanent Magnetization (IRM) were conducted in a magnetically shielded room at CEREGE using a cryogenic superconducting rock magnetometer (SRM) 760 (2G Enterprises) with a 46 mm bore and in-line degaussers, sensitive to 10^{-11} Am^2. The process included 22 incremental thermal steps from room temperature to 800°C, utilizing a TD48SC furnace (ASC Scientific). This method aimed to reduce magnetic remanence stepwise, providing insights into the coercivity distribution, unblocking temperatures, thermal stability, and magnetic phase composition. Isothermal remanent magnetization (IRM) was also thermally demagnetized using the same setup after pulse magnetization to 3.0 Tesla with a MMPM9 pulse magnetizer (Magnetic Measurements). The sample underwent alternating field (AF) demagnetization at 200 mT using an LDA5 demagnetizer (Agico) to eliminate magnetite magnetization, isolating remanence from higher-coercivity minerals. It then underwent 23 thermal demagnetization steps with the TD48SC furnace.

Samples of the carbonate fault mirror and fault core were oriented in the field using a magnetic compass for measurements of the anisotropy of anhysteretic remanent magnetization (AARM). The AARM was measured on 3.5 mm cubes to assess deformation-related changes. The maximum, intermediate, and minimum axes of the AARM ellipsoid are respectively referred to as J_1, J_2 and J_3. AARM of 32 oriented cubes (3.5 mm) were measured from two rock samples along the fault mirror using first an alternating demagnetizing field (AF) with a peak field of 200 mT and an applied DC magnetic field of 400 μT along predefined axes. An anhysteretic remanent magnetization (ARM) was imparted and measured along 15 directions: three primary axes (X, Y, Z), six diagonal directions (*e.g.*, X-Y, X-Z, Y-Z), and six intermediate angles (*e.g.*, 30° and 60°) according to Jelinek (1981) protocol. After inducing ARM, remanent magnetization was measured for each sample using the SRM. The AARM tensor was calculated from the intensity and direction of remanent magnetization in all 15 orientations to compare magnetization intensities using the Jelínek (1981) method. Eigenvalues and eigenvectors were used to define the principal axes of remanent anisotropy (J_1, J_2, J_3), thereby characterizing the magnetic anisotropy ellipsoid. Its shape and orientation aid in interpreting seismic deformation on the fault mirror. Data bootstrapping was employed to estimate sampling distribution, reduce bias and enhance visualization of AARM data.

Magnetic hysteresis measurements were conducted with a Vibrating Sample Magnetometer (VSM) 8604 (LakeShore Cryotronics), at fields up to 1 T, on fault mirror samples weighing 130 to 1300 mg. FORCInel v.3.08 (Harrison and Feinberg, 2008) was used to process and display First Order Reversal Curve (FORC) data.

AF demagnetization of NRM and IRM were performed using the SRM in 13 steps, with alternating fields increasing from 0 to 70 mT at room temperature in a magnetically shielded environment. The magnetic moment was measured to monitor changes in direction and magnitude of remanence, allowing for progressive reduction of remanent magnetization. For IRM demagnetization, rock samples weighing ~5 g were pulse magnetized to 3 Tesla using a MMPM9 impulse magnetizer. These samples also underwent 13 demagnetization steps up to 70 mT.

In addition, a fully automated, high-resolution uniaxial fluxgate scanner measured uniaxial magnetic fields on a 12 mm-long slab cut perpendicular to the fault mirror at a spatial resolution of 5.8 μm. These measurements were not performed in a magnetically shielded environment. The sample was previously magnetized using Helmholtz coils at 0.6 T. The setup included a fluxgate magnetometer positioned at 2 mm distance from the sample to accurately capture local fields from remanent magnetization (details in Demory et al., 2019).

The numerical modeling of frictional heat accounts for the heat sink effect of decarbonation reactions ($\Delta H = 187 \,.\, 10^3$ J/mol). Other modeling methodological details are in Zamani et al. (2025).

4. Results

4.1. Photogrammetric and TLS surveys

Drone photography (Figure 2) provides real-time orthographic imagery of the entire Santilli quarry which is used to identify large-scale fracture patterns and faults as well as local variations in the strike and dip of the Venere Fault. The main fault plane (Figures 2 and 3A) presents multiple patches where the glossy part of the principal slip surface was preserved, particularly toward the bottom third of this natural exposure. Eyewitnesses and historical photographs (*e.g.*, Serva et al., 1986; Amoroso et al., 2016) attest that the 1915 rupture produced a ~0.8 m displacement along this specific fault scarp. Removal of loose sediment by the quarry owner lead to the lighter color of the bottom left exposure. The outcrop greyish color results from weathering by atmospheric agents whereas the brownish color likely originates from soil formation.

The TLS data (Figure 3B) provides a structural map of the fault mirror at very high resolution (~6 mm/pixel), which allows the visualization of morphological details otherwise unnoticed with the naked eye. This survey shows that the exposed fault plane has a remarkably consistent dip angle (45 ± 12º) and a more variable dip direction (209 ± 17º) (Figure 3). The NW side of the exposed fault scarp has a generally shallower dip angle of ~35-50º than the SE side (~50-65º) while the dip angle varies from NNW on the NW side to WSW on the SE side (Figure 3C). The field-measured mean stretching lineation (slickensides) trends N212º with a 42º plunge (Figure 2), which is in agreement with the TLS-computed mean dip direction that trends at N209º, with a mean dip angle of 45º (Figure 3B). The roughness map (Suppl. Mat. Figure 3) shows an overall smooth surface with a roughness <0.005 m and a few patches, < 1 m in size, of higher roughness. The variations in dip directions show that the fault plane exhibits warping / undulations with an axis along the dip direction.

4.2. Macroscopic and microscopic structures

At the Santilli quarry, the Venere Fault plane exposes a surface with distinctively shiny patches and pervasive downdip shear sense indicators and slickensides that constitute the fault mirror (Figure 3E). In places, this >2-3 mm-thick fault mirror also shows reddish hematite-goethite striations parallel to the slickensides (Figure 3F and G). The streak of these minerals on the carbonates of the fault plane are reddish-brown and to yellow-brown. The slickenside asymmetry indicates a consistent normal slip sense. In the investigated fault core, we did not observe any evidence of the pressure-solution seams previously reported by Agosta and Aydin (2006). Also, hematite and goethite occur only along the fault mirror but were not observed in the fault core.

At the microscopic scale, the host carbonate presents abundant and remarkably well preserved ooids (Figures 4B and 4C) and a few planktonic foraminifera, genus *Globigerina*. The remarkable preservation of these sedimentary particles and microfossils highlights the strong strain partitioning between the fault mirror and the rest of the rock. The footwall fault core immediately adjacent to the fault mirror (zone Z_1) shows a 10-80 μm thick comminuted zone Z_1 in which clasts are less abundant than in the underlying zone Z_2 (Figures 4A and B). The Z_1 zone shows a distinct orangish coloration, parallel to the mirror, produced by opaque grains of disseminated iron oxides and hydroxides. This coloration gradually fades away from the mirror. Z_2 porosity consists of irregularly-shaped vugular pores locally showing a shape preferred orientation (SPO) parallel to the fault mirror (Figures 4D and 4E). The width of Z_2 ranges from 300 to 600 μm overall parallel to the fault mirror. The material from Z_1 locally forms injection fingers that cut sharply through Z_2 (Figure 4C). While the cause of the locally high porosity in Z_2 remains unknown, its spatial distribution and parallelism with the fault plane points to a previously unreported structural control. In these carbonates, energy dispersive spectroscopy (EDS) shows that opaque minerals form relatively small (~1 μm) and scarce, subequant isolated grains that consist exclusively of pure magnetite (no sulfides).

4.3. Magnetic susceptibility

The bulk magnetic susceptibility K_m of the Venere Fault rocks is reported in Table 1. For the undeformed footwall limestone, K_m was measured on ten samples away from the fault mirror, and ranges from -5.17 to –2.27 ± -1.0 × 10^{-6} [SI] with an average of -3.01 ± 0.90 × 10^{-6} [SI]. For the fault core, K_m was measured on 9 representative samples, at a distance <20 cm from the fault mirror, and ranges from -7.88 to -1.22 ± -0.9 × 10^{-6} [SI] with an average of -3.61 ± -0.3 × 10^{-6} [SI]. For the fault mirror, K_m was measured on 2 representative samples and ranges from 2.30 to 7.95 × 10^{-6} [SI] with an average of 5.13 ± 2.8 × 10^{-6} [SI]. These results show that the magnetic susceptibility of the fault rocks increases markedly towards the fault mirror and that K_m is systematically higher than that of pure calcite. Measurement of the anisotropy of magnetic susceptibility of these materials was attempted on oriented cubes (3.5 mm) using an Agico MFK1 Kappabridge instrument but did not yield reproducible results because the anisotropy is dominated by diamagnetic calcite and below the detection limit of the instrument.

4.4. Magnetic hysteresis

The magnetic hysteresis parameters were measured on representative samples of fault mirror (VEN04, VEN06) and fault core (VEN07) (Table 2; Suppl. Mat. Figure 1B). The contribution of paramagnetic phases was not determined due to large variability in high-field slope between samples and the dominant diamagnetic contribution.

For the fault core, saturation magnetization (M_s) ranges from 143 to 535 × 10^{-6} Am^2/kg, with an average of 339 ± 276 × 10^{-6} Am^2/kg, and the saturation magnetic remanence (M_r) ranges from 18 to 35 × 10^{-6} Am^2/kg, with an average of 26.5 ± 10.2 × 10^{-6} Am^2/kg. The magnetic coercivity (H_c) ranges from 6.2 to 6.7 mT, with an average of 6.45 ± 1.98 × 10^{-6} Am^2/kg, and the coercivity of remanence (H_{cr}) ranges from 25.9 to 27.8 mT, with an average of 26.9 ± 1.5 mT.

For the fault mirror, saturation magnetization (M_s) ranges from 68 to 945 × 10^{-6} Am^2/kg, with an average of 332 ± 276 × 10^{-6} Am^2/kg, and the saturation magnetic remanence (M_r) ranges from 11 to 151 × 10^{-6} Am^2/kg, with an average of 44.6 ± 25.0 × 10^{-6} Am^2/kg. The magnetic coercivity (H_c) ranges from 7.0 to 12 mT, with an average of 8.94 ± 1.77 × 10^{-6} Am^2/kg, and the coercivity of remanence (H_{cr}) ranges from 24.3 to 30.5 mT, with an average of 26.9 ± 1.4 mT.

These results are consistent with the >6 fold increase in magnetic remanence, measured from the fault core towards the fault mirror, through scanning of VEN04 (Figure 5A).

The FORC diagram for the fault mirror (Suppl. Mat. Figure 1A) shows a superparamagnetic fringe close and parallel to the B_u axis consistent with presence of nanoscale magnetite and a ridge-shape region parallel to the B_c axis produced by fine-grained hematite or goethite. The IRM deconvolution (Suppl. Mat. Figure 1D) documents two phases of distinct mean coercivities, Bh_1 (~335 mT) and Bh_2 (>3.0 T), hence supporting the FORC results.

4.5. Thermal and AF demagnetization of NRM and IRM

The AF demagnetization of NRM experiments on VEN06 shows a progressive, smooth decrease in magnetic remanence from 2 to 60 mT, indicative of the presence of low-coercivity component, such as low-Ti content magnetite (Suppl. Mat. 2A). The remanence jump at 440ºC is considered a spurious instrument measurement. The AF demagnetization of IRM experiments performed on an aliquot specimen of VEN06 (Figure 5B) confirms the smooth and progressive demagnetization behavior between 2 and 60 mT, which is typical of magnetite.

The thermal demagnetization of NRM experiments on VEN06 shows a ~50% drop in magnetic remanence below 120ºC, indicative of the presence of goethite, followed by a lack of consistent demagnetization between 150 and 600ºC, followed by a ~40% loss of magnetization between 600 and 700ºC, indicative of the presence of low-Ti content hematite or maghemite (Suppl. Mat. 2B). The thermal demagnetization of IRM experiments on VEN06 (Figure 5C) shows a ~40% drop in magnetic remanence below 120ºC, confirming the presence of goethite, followed by a smooth demagnetization between 120 and 600ºC, and ultimately a minor loss of magnetization (~5%) between 600 and 700ºC, which indicates that the magnetization of the high unblocking temperature phase (maghemite or hematite) was not effectively boosted by the IRM.

4.6. AARM directional results

The AARM samples of this study (VEN04 and VEN06) were both collected in a straight and representative segment of the fault (Figure 2). The AARM data (Table 3, Figure 6) shows relatively small remanent magnetization ~0.7 ± 0.1 × 10^{-6} Am^2 for VEN04 and ~2 ± 0.1 × 10^{-6} Am^2 for VEN06. These experiments show that the AARM long axes (J_1), *i.e.*, AARM magnetic lineation, are scattered due to the low magnetic mineral content of these carbonates (~0.5 ppm of magnetite, Tables 2 and 3) and define a partial girdle parallel to the fault plane (Figure 6A, B, F and G). Despite the scatter of the individual J_1 directions, it is noteworthy that the tensorial mean J_1 statistically plots within 10º of the mineral striations / slickensides along the fault mirror. As shown by the bootstrapped data, *i.e.*, higher clustering, the statistical significance of the AARM fabric improves when the sample number increases from 12 to 20. The mean J_3 axis (pole to the AARM planar fabric) plots within 10º to the pole of the fault plane. The degree of AARM (P') does not correlate with J_{mean} (Figure 6C and H) or the AARM shape parameter, T (Figure 6D and I). Overall, the symmetry of the AARM fabric is neither prolate nor oblate (Figure 6D and I).

5. Discussion

5.1. Significance of carbonate fault mirrors with respect to seismic deformation

In carbonates, and many other rocks, faults tend to have a consistent architecture characterized by juxtaposed zones with progressively increasing deformation from the undeformed bedrock (*e.g.*, Fossen, 2010) . The least deformed zone in general referred to as the damage zone, shows a gradual increase of fracture density towards the most deformed zone. The most deformed zone, referred to as fault core, exhibits intense fracturing and, in carbonates, generally consists of cataclasite to ultracataclasite. In many cases, a discrete zone within the fault core referred to as a principal slip plane account for large displacement over a relatively thin domain. The principal slip zone is generally coated with slickensides, slickenlines and striated minerals. In some cases, this slip zone exhibits a highly reflective surface named a fault mirror. The fault architecture is overall symmetrical with respect to the fault mirror, therefore the damage zone exists both in the footwall and hanging wall. In carbonate rocks, fault mirrors owe their high optical reflectance to nano-sized calcite grains (<1 μm) (*e.g.*, Han et al., 2007a,b; Fondriest et al., 2013; Siman-Tov et al., 2013; Ohl et al., 2020). As shown by deformation experiments, these fault mirrors are produced by two distinct processes: i) Frictional heating leading to decarbonation and recrystallization of lime into nano-calcite (Han et al., 2007a,b; Carpenter et al., 2015), and ii) ultra-comminution, coupled with frictional-heating-induced sintering (Storti et al., 2003; Billi and Storti, 2004; Pozzi et al., 2018).

Recent studies suggest that carbonate-hosted fault mirrors predominantly form during slip at seismic velocities (0.1 to 10 m/s), making them potential indicators of paleoseismic activity (Siman-Tov et al., 2013; 2015; Kuo et al., 2016; Ohl et al., 2020). In the case of the Venere Fault, mirror formation is directly linked to the 1915 seismic event. This raises the key question of whether frictional heating or decarbonation is the dominant cause of fault mirror development?

5.2. *Photogrammetric and TLS contributions to structural analysis of the Venere Fault*

The analysis of coseismic deformation along natural seismogenic fault surface requires field observations, at multiple scale, due to the large number of parameters that may affect seismic rupture. At the kilometer scale, changes in seismic slip length may cause substantial variations in the nature of macroscopic rupture indicators (*e.g.*, Del Sole et al., 2025). At the meter scale, variations in dip angle may also result in profound differences in coseismic frictional heat (*e.g.*, Zamani et al., 2025). At the microscopic scale, differences in rock composition lead to activation of distinct deformation mechanisms (*e.g.*, Smeraglia et al., 2017). TLS data provides insights on deformation processes across several scales at once. The TLS data (Figure 3B) shows that the mirror has a consistent strike and dip, except on the SE side of the scarp where it becomes more southerly. The short-wavelength variations in dip direction along the fault plane (Figure 3), form an asymmetric draping structure, parallel to the dip direction, that probably results from the previously documented, minor right-lateral strike-slip component of the fault (*e.g.*, Agosta and Kirchner, 2003). These steps resemble, albeit on a macroscopic scale, of the step fractures kinematic indicators described by Doblas (1988). The TLS method is also utilized to compute fault roughness parallel to slip direction using Renard and Candella (2017)'s method. The roughness map (Suppl. Mat. Figure 3) reveals patches of higher roughness, with no preferred orientation or shape. Overall, the roughness of the NW third length of the scarp is less than its central and SE parts. Also, the apparently strong correlation between roughness (Suppl. Mat. Figure 3) and dip angle (Figure 3C) will be further discussed in a subsequent investigation (Nováková et al., in preparation). Finally, the Venere fault plane does not show major structural asperities along the down-dip slip direction, which supports that this is a mature fault that experienced at least four previous ruptures (see section 2).

5.3. *Numerical quantification of frictional heat*

The quantification of frictional heat, and possible ensuing decarbonation, are discussed along with several characteristics of coseismic slip, including grain size reduction, fluid flow, and fault plane geometry. The TLS data was used to quantify frictional heat (Q_f) along the fault plane (Table 4; Figure 3C). The change of enthalpy ($\Delta H = 187 \times 10^3$ J/mol) associated with decarbonation is taken from Humphries et al. (2019), a value that generally applies to thermal decomposition of calcite. Additional calculation details are provided in Zamani et al. (2025). These calculations show that, with an estimated slip of 0.8 m, due to the modest depth at which the fault scarp was during the 1915 Avezzano earthquake, the normal stress on the fault plane was most likely a minimal value and decarbonation would have affected a less than 2 μm-thick layer of carbonate (Table 4). Because this value is about three orders of magnitude smaller than the fault roughness, decarbonation would have taken place along the Venere fault mirror only in patches corresponding to asperities or to areas of shallower dip. Despite the fact that the extent of decarbonation was most likely limited, some microstructures (Figure 4 D and E) resemble those produced in friction-experiments where decarbonation was observed (*e.g.*, Aretusini et al., 2024; Violay et al., 2013).

5.4. Previous magnetic investigations on fault rocks and contributions to magnetic susceptibility

Earlier studies on fault rocks established the great potential of magnetic studies for deformation analysis arising from their high sensitivity to minute physical, thermal and mineralogical changes (*e.g.*, Borradaile and Jackson, 2004; Levi et al., 2014; Yang et al., 2020). The main challenge in measuring the anisotropy of magnetic susceptibility (AMS) of diamagnetic rocks, such as quartzites, limestones, or dolomites, lies in the weakness of their magnetic susceptibility, combined with the competition between their diamagnetic and minor para- or ferromagnetic contributions (Hrouda et al., 2004; Martín-Hernández and Ferré, 2007; Schmidt et al., 2007; Almqvist et al., 2009; Levi and Weinberger, 2011; Issachar et al., 2018; Biedermann et al., 2020; Zamani et al., 2023).

Another difficulty in isolating the fabric of fault rocks is the standard specimen size generally required for magnetic measurements, which typically is 2.5 cm diameter cores (*e.g.*, Tarling and Hrouda, 1993; Molina-Garza et al., 2009). This size requirement put limitations on the scale at which deformation can be quantified. Nonetheless, improvements in instrumentation sensitivity recently allowed the anisotropy of magnetic susceptibility measurement of smaller rock volumes of ca. 40 mm^3 (Ferré et al., 2016; Zamanialavijeh et al., 2021; Zhang et al., 2024). In the present study, the very high sensitivity of SQUID magnetometers is used to push the detection limit of seismogenic fabrics by performing AARM measurements on 3.5 mm cubes of quasi-pure platform carbonates containing less than 1 ppm of magnetite.

At the Santilli quarry, the Venere Fault host-carbonates consist of 99.99 % calcite (Table 1). Using this percentage and the intrinsic magnetic susceptibility of pure calcite (Schmidt et al., 2006), the diamagnetic contribution is calculated as $K_{dia} = -12.08 \pm 0.5 \times 10^{-6}$ [SI]. The paramagnetic contribution, determined from the high-field slope of magnetic hysteresis experiments after diamagnetic correction, is $K_{para} = 0.456 \pm 0.005 \times 10^{-6}$ [SI]. This small contribution attests to the paucity of paramagnetic phases such as clays, sulfides or iron hydroxides (*e.g.*, γFeOOH) in the limestone. The ferromagnetic contribution to magnetic susceptibility is overall minor, ~8.62, 8.02 and 16.75 × 10^{-6} [SI] respectively in the undeformed limestone, fault core and fault mirror (Table 1). Thermal and AF demagnetization experiments along with IRM acquisition results indicate that magnetite is the dominant ferromagnetic phase in these rocks with contributions from goethite and hematite to magnetic remanence being <1% (Figure 5 B and C).

The presence of magnetite, albeit in trace amounts, in the white, undeformed limestone, is interpreted as evidence for a sedimentary origin. In similar platform carbonates, magnetite typically originates from bacterial (*e.g.*, Arakaki et al., 2008; Roberts et al., 2013) or atmospheric detrital sources (*e.g.*, Dinarès-Turell et al., 2003; Hladil et al., 2006). The specific origin of this sedimentary magnetite remains to be determined. Based on the respective contributions of diamagnetic, paramagnetic and ferromagnetic minerals to magnetic susceptibility (Table 1), the AARM arises most likely from shape-preferred orientation (SPO) of magnetite grains.

5.5. Origin of the magnetic mineral assemblage and AARM significance

The anisotropy of anhysteretic remanent magnetization isolates the ferromagnetic contribution to magnetic fabric of rocks, particularly in the case of weakly magnetic carbonates (*e.g.*, McCabe and Jackson, 1985; Aubourg and Robion, 2002; Evans et al., 2003; Borradaile and Jackson, 2010; Hirt and Almqvist, 2012; Bilardello and Jackson, 2014; Levi et al., 2014; Casas-Sainz et al., 2017; Issachar et al., 2018; Biedermann et al., 2018; 2020a, b; Mattsson et al., 2021). These studies also show that in most carbonates, magnetite is the dominant carrier of remanence and AARM. In undeformed carbonates, that have not been remagnetized by fluids, the AARM arises primarily from depositional processes (*e.g.*, Parés et al., 2015). In contrast, in deformed carbonates, the AARM may arise from authigenic magnetite in pressure-solution structures (*e.g.*, Evans and Elmore, 2006).

In the Venere Fault carbonates of the Santilli quarry, the presence of preseismic magnetite is documented through SEM observations (Figure 4), magnetic hysteresis properties (Suppl. Mat. Figure 1B), IRM deconvolution and thermal and AF demagnetization behavior (Figure 5B). In addition, at the Santilli quarry, hematite and goethite do not occur away from the fault mirror where they form slickenlines (Figure 3 F, G, H and I). These two phases must have formed respectively through oxidation and hydration of prior magnetite in the high porosity (ϕ)– high permeability (k) zone along the fault core-fault damage boundary documented by Agosta and Aydin (2006), Agosta et al. (2007) and Agosta (2008). The same authors also describe the fault mirror as a hydraulic barrier, along which fluid flow would be unlikely. Therefore, we conclude that magnetite oxidation and hydration predates seismic slip, and that hematite and goethite from the fault core were smeared during the 1915 Avezzano earthquake to form slickensides along the fault mirror. However, we note that the 1915 Avezzano earthquake might have been triggered by fluid pressure variations at depth related to the Fucino Lake, as this lake was completed in 1878 (*e.g.*, Robinson et al., 1915; Boncio et al., 2016; Di Naccio et al., 2020).

As attested by multiple eyewitnesses (*e.g.*, Serva et al., 1986; Amoroso et al., 2016), the ~0.8 m-high fault mirror at the Santilli quarry unarguably formed during the 1915 Avezzano earthquake. The hematite and goethite slickensides, that are exclusively present on this fault mirror, must, therefore, have been produced during the 1915 seismic slip event. As magnetite formation predates seismic slip and its magnetic fabric (AARM) coincides with slickensides, we conclude that it acquired a new shape fabric during coseismic slip by a deformation mechanism yet to be determined. The AARM shape factor (neither prolate nor oblate) and the high strain rate / low-temperature of coseismic deformation, together support the rotation of magnetite grains as passive markers in cataclastic flow rather than a mechanism involving grain plasticity.

The respective contributions of magnetite, hematite, and goethite to AARM remains unclear but, based on the deconvolution of IRM acquisition, magnetite overwhelms the magnetic remanence and therefore probably also dominates the AARM.

The interpretation that the AARM fabric mimics coseismic deformation is strongly supported by the near coaxiality of the AARM principal axes with the fault plane, *i.e.*, pole to fault plane: N029º, 46º; AARM J_3: N032º, 30º for VEN06, and N039º, 32º for VEN04 (Figure 6). Also, the slickensides (N210º, 43º) coincide with the AARM J_1 axes, *i.e.*, N208º, 60º for VEN06 and N154º, 34º for VEN04 (Figure 6). These remarkable results highlight the potential of the AARM approach to analyze coseismic deformation at a high resolution. Our attempts to further characterize the shape of magnetite grains using scanning electron microscopy did not yield convincing results due to the scarcity of grains and their small sizes (generally <500 nm).

Previous studies have shown that the AMS method can quantify deformation at seismic slip rates using 3.5 mm cubes (*e.g.*, Ferré et al., 2015, 2016; Zamanialavijeh et al., 2021; Zhang et al., 2024; Zamani et al., 2025). In the case of the Venere Fault, the ferromagnetic mineral content is too low ($K_m < 100 \times 10^{-6}$ [SI]) for the AMS method to be used. In other cases of fault rocks where carbonates are iron-rich, such as for example the Hebgen Lake Fault in Montana (*e.g.*, Zamani et al., 2025), the AMS accurately records the direction of seismic slip. Finally, this study highlights the potential of AARM to quantify seismic deformation in materials that are too weakly magnetic to exhibit a meaningful AMS, such as pure carbonates, or when the ferromagnetic contribution to AMS is too weak (*e.g.*, Almqvist et al., 2020).

5.6. Implications of this study for coseismic decarbonation and deformation

In general, the distribution of frictional heat on natural fault planes tends to be heterogeneous which ultimately results in flash heating on asperities *(e.g.*, Rice, 2017). However, in the case of the Venere Fault, the widespread preservation of goethite along the fault mirror attests that overall frictional heating did not reach the temperature required for goethite to hematite reaction, which is between 400 and 600ºC (Gialanella et al., 2010; Ponomar, 2018; Walter et al., 2001). This is also confirmed by thermal demagnetization experiments that confirm the persistence of goethite along the fault mirror (Figure 5 and Suppl. Fig. 2). Hence, we demonstrate that the magnetic fabric of the fault mirror developed during seismic slip under moderate thermal conditions (<400ºC). These thermal conditions are generally not linked to fault weakening due to decarbonation, which in turn has implications for rupture propagation and seismic hazard assessment (*e.g.*, Del Sole et al., 2024). The moderate thermal conditions inferred from the magnetic study are also consistent with the development of injection fingers (Figure 4C) that attests of coseismic fluidization due to ultracataclasic comminution.

Balsamo et al. (2014) also suggested that, as grain-size, porosity and permeability jointly decrease during increasing deformation, above a certain fabric threshold, coseismic rupture can propagate along the shallow portions of creeping extensional faults, including through unconsolidated sediments. This is most likely the case for the Venere Fault. We interpret the exposed fault mirror at the Santilli quarry as evidence of slip propagating upward along an extensional fault.

Finally, based on the empirical relationships by Wells and Coppersmith (1994) between surface rupture length (SRL) and displacement (D), as well as SRL and moment magnitude (Mw) for normal faults, the 1915 Venere Fault rupture produced a larger magnitude earthquake than predicted and a shorter surface rupture than expected. We propose that either the displacement was significantly larger than observed at the Santilli quarry, possibly due to slip partitioning, or that, as shown elsewhere, the earthquake magnitude could have been amplified if the rupture reached supershear speed (Bao et al., 2022; Ren et al., 2024).

6. Conclusion

Our study provides new insights into seismic slip processes along carbonate-hosted faults, using the Venere Fault, in the Fucino Basin, as a natural laboratory. The exceptionally well-preserved fault mirror at the Santilli Quarry, formed during the 1915 Avezzano M_W 7.0 earthquake, serves as direct evidence of seismogenic slip in carbonate rocks. Through an integrated analysis of structural mapping, microstructural observations, magnetic methods, and thermal modeling, we demonstrate that the mirror formed primarily through extreme grain-size reduction rather than widespread decarbonation.

Terrestrial laser survey data highlights a fault surface with limited large-scale asperities and a draping structure that suggests minor right-lateral kinematics in addition to dip-slip motion. Frictional heating appears moderate (<400°C), as evidenced by the preservation of goethite and the absence of pervasive decarbonation microstructures. These findings challenge the assumption that decarbonation would be a dominant weakening mechanism in seismogenic carbonate-hosted faults, at least in this case, and suggest that ultracomminution and localized fluidization may play a more significant role.

Magnetic analyses further reveal that magnetite is the primary carrier of remanence, with the anisotropy of anhysteretic remanent magnetization (AARM) effectively capturing, for the first time, the coseismic kinematics of the fault mirror. These results underscore the potential of AARM as a high-resolution tool for detecting seismic fabrics in carbonate fault zones, even when the conventional anisotropy of magnetic susceptibility (AMS) method is ineffective due to weak magnetic susceptibility.

By integrating field and laboratory observations with numerical modeling, our study advances the understanding of seismic slip in carbonate faults, emphasizing the need for multi-scale investigations. The findings have important implications for seismic hazard assessment, as they highlight the complex interplay of frictional heating, grain-size reduction, and fluid-rock interactions in controlling fault weakening mechanisms and rupture propagation.

Acknowledgements

We thank Mr. Santilli for kindly providing access to the quarry and Dr. Alessio Testa for his assistance during field data and sample collection. All figures were created using Adobe Illustrator v.29.0 and Arc-GIS Pro v.3.2 (for Figure 1). NZ is grateful for the Chateaubriand Fellowship received from the French Embassy in the United States during which she was hosted at CEREGE for four months in the framework of this award. We are thankful to the Editor, Jianhua Li, Associate Editor, Gaetan Milesi, for their positive feedback to this manuscript. We acknowledge the excellent scientific reviews by Andrea Billi and an anonymous reviewer.

List of Figures

Figure 1. Elevation map of the Fucino Basin with main regional faults and related focal mechanisms (after Cella et al., 2021 and Volatili et al., 2022). The location of the study area is shown by the red square.

Figure 2. Satellite image of the Santilli quarry showing the main normal and transverse faults, magnetic sample locations and rose diagrams of slickensides.

Figure 3. A – Drone orthophotograph of the main Venere Fault scarp at the Santilli quarry, projected on the fault plane. The black line shows areas excluded from the structural analysis due to surface artefacts including loose sediments, gravel, etc. B – Stereographic projections of fault plane attitudes computed from Lidar TLS survey (n > 23 x 10^6 points). C – TLS map of dip angles with a resolution of 6 mm per measurement. D – TLS map of dip direction (same resolution as C); the variations in dip directions show that the fault plane exhibits warping / undulations with an axis along the dip direction. This asymmetric geometry is interpreted as resulting from synkinematic right-lateral folding of the fault plane. E – Oblique view of the Venere Fault showing atmospheric alteration of the carbonate (black color) and gravel cover. The fault core (breccia) locally forms a ~0.3 m-thick zone below the fault mirror (fm). F – Outcrop-scale view of the iron oxide-hydroxide slickensides. G – Close-up view of the slickensides. H – Transverse macroscopic view of the fault mirror showing the reddish-orangish thin zone of the fault mirror. I – Calcite and goethite striations on the fault mirror with fine-grained calcite powder.

Figure 4. Optical (OPT) and scanning electron microscopy (SEM) images showing on grain sizes and deformation microstructures in the Venere Fault mirror. A – OPT - VEN06 section

perpendicular to fault mirror illustrating < 5mm-thick iron oxide-rich fault mirror, presence of vugs possibly resulting from local decarbonation and coseismic Riedel fractures. B – SEM image documenting the irregular vugs and a band of plastic, HT deformed calcite parallel to mirror. C – OPT – Ooliths showing preservation of sedimentary microstructures, carbonate ultracataclasite injection vein and angular clasts. D – Local development of nanocalcite possibly suggestive of decarbonation. E – OPT F – OPT- VEN07 high porosity sheared domain with small goethite-rich. G – OPT – Fault mirror microstructures. - Flow direction of granular material. H – OPT - Relatively undeformed ooid-rich subdomains (clasts) with carbonate ultracataclasite.

Figure 5. Magnetic data of the Venere Fault supporting the presence of magnetic remanence carriers. A – Scan showing distinct increase in magnetic remanence towards the fault mirror. The purple square on the left represents the average NRM of 3.5 cubes ~10 mm away from the fault mirror ($J_{NRM} = 1.24 \times 10^{-8}$ A/m) whereas the red square is for cubes ~ 2 mm away from the fault mirror (~25.4×10^{-8} A/m), hence showing the increase in NRM towards the mirror. B – Alternating field (AF) demagnetization of isothermal remanent magnetization (IRM, 3 T) showing a smooth demagnetization behavior characteristic of low coercivity phase. C – Thermal demagnetization of IRM (3 T) showing loss of magnetization below 120ºC, continuous demagnetization from 120 to 575ºC, followed by drop in magnetization above 600ºC.

Figure 6. Anisotropy of anhysteretic remanent magnetization (AARM) for two fault mirror samples: VEN04 (A→E) and VEN06 (F→J). A and F, stereographic projections of AARM principal axes. B and G, bootstrapped data. C and H, P' vs J_{mean} diagrams. D and I, T vs P' diagram. E and J, histograms showing distribution of J_{mean} values.

List of Tables

Table 1. Mineral composition from XRD and bulk magnetic susceptibility of the Venere Fault rocks.

Table 2. Magnetic hysteresis parameters of the Venere Fault rocks (mirror).

Table 3. Anisotropy of anhysteretic remanent magnetization (AARM) of the Venere Fault mirror (VEN06).

Table 4. Parameters, units, and equations of frictional heat on the Venere Fault plane.

Supplementary Material

Supplemental Material - Figure 1. A - First order reversal curve (FORC) diagram showing a superparamagnetic fringe ridge-shape region parallel to the B_c axis. B – Dunlop (2002) plot of magnetic hysteresis ratios M_r/M_s vs H_{cr}/H_c. C – Isothermal remanent magnetization (IRM) acquisition. D - Deconvolution of isothermal remanent magnetization (IRM) acquisition using *MaxUnmix* showing two components of magnetic remanence with distinct mean coercivities, Bh_1 (~335 mT) and Bh_2 (>3.0 T).

Supplemental Material – Figure 2. Representative stepwise demagnetization experiments of natural remanent magnetization (NRM). A - AF demagnetization of NRM. B. Thermal demagnetization of NRM.

Supplemental Material – Figure 3. Roughness map produced from the TLS data.

References

Agosta, F., 2008. Fluid flow properties of basin-bounding normal faults in platform carbonates, Fucino Basin, central Italy. Geological Society, London, Special Publications, 299(1), pp.277-291.

Agosta, F., Prasad, M. and Aydin, A., 2007. Physical properties of carbonate fault rocks, Fucino basin (Central Italy): implications for fault seal in platform carbonates. *Geofluids*, *7*(1), pp.19-32.

Agosta, F. and Aydin, A., 2006. Architecture and deformation mechanism of a basin-bounding normal fault in Mesozoic platform carbonates, central Italy. Journal of Structural Geology, 28(8), pp.1445-1467.

Agosta, F., Kirschner, D.L., 2003. Fluid conduits in carbonate-hosted seismogenic normal faults of central Italy. Journal of Geophysical Research: Solid Earth, 108(B4).

Agosta, F., Prasad, M. and Aydin, A., 2007. Physical properties of carbonate fault rocks, Fucino basin (Central Italy): implications for fault seal in platform carbonates. Geofluids, 7(1), pp.19-32.

Agosta, F. and Kirschner, D.L., 2001. Stable isotope evidence for contrasting paleofluid circulation in thrust faults and normal faults of the central Apennines, Italy. Journal of Geophysical Research: Solid Earth, 106(B5), pp.8811-8825.

Almqvist, B.S., Bender, H., Bergman, A. and Ring, U., 2020. Magnetic properties of pseudotachylytes from western Jämtland, central Swedish Caledonides. *Solid Earth*, *11*(3), pp.807-828.

Almqvist, B.S., Hirt, A.M., Schmidt, V. and Dietrich, D., 2009. Magnetic fabrics of the Morcles Nappe complex. *Tectonophysics*, *466*(1-2), pp.89-100.

Amoroso, S., Bernardini, F., Blumetti, A.M., Civico, R., Doglioni, C., Galadini, F., Galli, P., Graziani, L., Guerrieri, L., Messina, P. and Michetti, A.M., 2016. Quaternary geology

Arakaki, A., Nakazawa, H., Nemoto, M., Mori, T. and Matsunaga, T., 2008. Formation of magnetite by bacteria and its application. *Journal of the Royal Society interface*, *5*(26), pp.977-999.

Aretusini, S., Nuñez Cascajero, A., Cornelio, C., Barrero Echevarria, X., Spagnuolo, E., Tapetado, A., Vazquez, C., Di Toro, G. and Cocco, M., 2024. Mechanical energy dissipation during seismic dynamic weakening in calcite-bearing faults. *Journal of Geophysical Research: Solid Earth*, *129*(9), p.e2024JB028927.

Aubourg, C. and Robion, P., 2002. Composite ferromagnetic fabrics (magnetite, greigite) measured by AMS and partial AARM in weakly strained sandstones from western Makran, Iran. *Geophysical Journal International*, *151*(3), pp.729-737.

Bao, H., Xu, L., Meng, L., Ampuero, J.P., Gao, L. and Zhang, H., 2022. Global frequency of oceanic and continental supershear earthquakes. *Nature Geoscience*, *15*(11), pp.942-949.

Balsamo, F., Aldega, L., De Paola, N., Faoro, I. and Storti, F., 2014. The signature and mechanics of earthquake ruptures along shallow creeping faults in poorly lithified sediments. Geology, 42(5), pp.435-438.

Bedford, J.D., Faulkner, D.R. and Lapusta, N., 2022. Fault rock heterogeneity can produce fault weakness and reduce fault stability. *Nature Communications*, 13(1), p.326.

Biedermann, A.R., Jackson, M., Stillinger, M.D., Bilardello, D. and Feinberg, J.M., 2020. Anisotropy of Full and Partial Anhysteretic Remanence Across Different Rock Types: 1—Are Partial Anhysteretic Remanence Anisotropy Tensors Additive?. *Tectonics*, *39*(2), p.e2018TC005284.

Biedermann, A.R., 2020. Current challenges and future developments in magnetic fabric research. *Tectonophysics*, *795*, p.228632.

Biedermann, A.R., 2018. Magnetic anisotropy in single crystals: A review. *Geosciences*, *8*(8), p.302.

Billi, A., Salvini, F. and Storti, F., 2003. The damage zone-fault core transition in carbonate rocks: implications for fault growth, structure and permeability. *Journal of Structural geology*, *25*(11), pp.1779-1794.

Bilardello, D. and Jackson, M.J., 2014. A comparative study of magnetic anisotropy measurement techniques in relation to rock-magnetic properties. *Tectonophysics*, *629*, pp.39-54.

Boncio, P., Dichiarante, A.M., Auciello, E., Saroli, M. and Stoppa, F., 2016. Normal faulting along the western side of the Matese Mountains: Implications for active tectonics in the Central Apennines (Italy). *Journal of Structural Geology*, *82*, pp.16-36.

Borradaile, G.J. and Jackson, M., 2010. Structural geology, petrofabrics and magnetic fabrics (AMS, AARM, AIRM). *Journal of Structural Geology*, *32*(10), pp.1519-1551.

Borradaile, G.J. and Jackson, M., 2004. Anisotropy of magnetic susceptibility (AMS): magnetic petrofabrics of deformed rocks. *Geological Society, London, Special Publications*, *238*(1), pp.299-360.

Brantut, N., Schubnel, A., Corvisier, J. and Sarout, J., 2010. Thermochemical pressurization of faults during coseismic slip. *Journal of Geophysical Research: Solid Earth*, 115(B5).

Bullock, R.J., De Paola, N., Holdsworth, R.E. and Trabucho-Alexandre, J., 2014. Lithological controls on the deformation mechanisms operating within carbonate-hosted faults during the seismic cycle. *Journal of Structural Geology*, 58, pp.22-42.

Carafa, M.M.C., Galvani, A., Di Naccio, D., Kastelic, V., Di Lorenzo, C., Miccolis, S., Sepe, V., Pietrantonio, G., Gizzi, C., Massucci, A. and Valensise, G., 2020. Partitioning the ongoing extension of the central Apennines (Italy): Fault slip rates and bulk deformation rates from geodetic and stress data. *Journal of Geophysical Research: Solid Earth*, *125*(7), p.e2019JB018956.

Carmignani, L. and Kligfield, R., 1990. Crustal extension in the Northern Apennines: the transition from compression to extension in the Alpi Apuane core complex. *Tectonics*, *9*(6), pp.1275-1303.

Carpenter, B.M., Mollo, S., Viti, C. and Collettini, C., 2015. Influence of calcite decarbonation on the frictional behavior of carbonate-bearing gouge: implications for the instability of volcanic flanks and fault slip. *Tectonophysics*, *658*, pp.128-136.

Casas-Sainz, A.M., Román-Berdiel, T., Oliva-Urcia, B., García-Lasanta, C., Villalaín, J.J., Aldega, L., Corrado, S., Caricchi, C., Invernizzi, C. and Osácar, M.C., 2017. Multidisciplinary approach to constrain kinematics of fault zones at shallow depths: a case study from the Cameros–Demanda thrust (North Spain). *International Journal of Earth Sciences*, *106*, pp.1023-1055.

Cavinato, G.P., Carusi, C., Dall'Asta, M., Miccadei, E. and Piacentini, T., 2002. Sedimentary and tectonic evolution of Plio–Pleistocene alluvial and lacustrine deposits of Fucino Basin (central Italy). *Sedimentary Geology*, *148*(1-2), pp.29-59.

Cella, F., Nappi, R., Paoletti, V. and Florio, G., 2021. Basement mapping of the Fucino Basin in Central Italy by ITRESC modeling of gravity data. *Geosciences*, *11*(10), p.398.

Cello, G., Mazzoli, S., Tondi, E. and Turco, E., 1997. Active tectonics in the central Apennines and possible implications for seismic hazard analysis in peninsular Italy. *Tectonophysics*, *272*(1), pp.43-68.

Chen, J., Niemeijer, A.R. and Spiers, C.J., 2021. Microphysical modeling of carbonate fault friction at slip rates spanning the full seismic cycle. *Journal of Geophysical Research: Solid Earth*, *126*(3), p.e2020JB021024.

Cornet, F.H., Doan, M.L., Moretti, I. and Borm, G., 2004. Drilling through the active Aigion Fault: the AIG10 well observatory. *Comptes Rendus. Geoscience*, 336(4-5), pp.395-406.

Cowie, P. A., R. J. Phillips, Gerald P. Roberts, K. McCaffrey, L. J. J. Zijerveld, L. C. Gregory, J. Faure Walker et al. "Orogen-scale uplift in the central Italian Apennines drives episodic behaviour of earthquake faults." *Scientific Reports* 7, no. 1 (2017): 44858.

Curzi, Manuel, Stefano M. Bernasconi, Andrea Billi, Chiara Boschi, Luca Aldega, Stefania Franchini, Richard Albert et al. "U-Pb age of the 2016 Amatrice earthquake causative fault (Mt. Gorzano, Italy) and paleo-fluid circulation during seismic cycles inferred from inter-and co-seismic calcite." *Tectonophysics* 819 (2021): 229076.

Del Sole, L., Vignaroli, G., Moretto, V., Curzi, M., Aldega, L., van der Lelij, R. and Viola, G., 2024. *A reappraisal of the Carboneras Fault (SE Spain) from new structural, geochronological and thermal constraints* (No. EGU24-11036). Copernicus Meetings.

Del Sole, L., Viola, G., Aldega, L., Moretto, V., Curzi, M., Xie, R., Cantelli, L. and Vignaroli, G., 2025. High-resolution investigations of fault architecture in space and time. *Scientific Reports*, *15*(1), p.2258.

Demory, F., Uehara, M., Quesnel, Y., Rochette, P., Romey, C., Tachikawa, K., Garcia, M., Borschneck, D., Pignol, L., Bard, E. and Andrieu-Ponel, V., 2019. A new high-resolution magnetic scanner for sedimentary sections. *Geochemistry, Geophysics, Geosystems*, *20*(7), pp.3186-3200.

Di Naccio, D., Famiani, D., Liberi, F., Boncio, P., Cara, F., De Santis, A., Di Giulio, G., Galadini, F., Milana, G., Rosatelli, G. and Vassallo, M., 2020. Site effects and widespread susceptibility to permanent coseismic deformation in the Avezzano town (Fucino basin, Central Italy): Constraints from detailed geological study. *Engineering Geology*, *270*, p.105583.

Dinarès-Turell, J., Baceta, J.I., Pujalte, V., Orue-Etxebarria, X., Bernaola, G. and Lorito, S., 2003. Untangling the Palaeocene climatic rhythm: an astronomically calibrated Early Palaeocene magnetostratigraphy and biostratigraphy at Zumaia (Basque basin, northern Spain). *Earth and Planetary Science Letters*, *216*(4), pp.483-500.

Di Toro, G., Han, R., Hirose, T., De Paola, N., Nielsen, S., Mizoguchi, K., Ferri, F., Cocco, M. and Shimamoto, T., 2011. Fault lubrication during earthquakes. *Nature*, 471(7339), pp.494-498.

Di Toro, G., Niemeijer, A., Tripoli, A., Nielsen, S., Di Felice, F., Scarlato, P., Spada, G., Alessandroni, R., Romeo, G., Di Stefano, G. and Smith, S., 2010. From field geology to earthquake simulation: a new state-of-the-art tool to investigate rock friction during the seismic cycle (SHIVA). Rendiconti Lincei, 21, pp.95-114.

Doblas, M., Oyarzun, R., Lunar, R., Mayor, N. and Martinez, J., 1988. Detachment faulting and late Paleozoic epithermal Ag-base-metal mineralization in the Spanish central system. *Geology*, *16*(9), pp.800-803.

Evans, M.A. and Elmore, R.D., 2006. Fluid control of localized mineral domains in limestone pressure solution structures. *Journal of Structural Geology*, *28*(2), pp.284-301.

Evans, M.A., Lewchuk, M.T. and Elmore, R.D., 2003. Strain partitioning of deformation mechanisms in limestones: examining the relationship of strain and anisotropy of magnetic susceptibility (AMS). *Journal of Structural Geology*, *25*(9), pp.1525-1549.

Fagereng, Å., Savage, H.M., Morgan, J.K., Wang, M., Meneghini, F., Barnes, P.M., Bell, R., Kitajima, H., McNamara, D.D., Saffer, D.M. and Wallace, L.M., 2019. Mixed deformation styles observed on a shallow subduction thrust, Hikurangi margin, New Zealand. Geology, 47(9), pp.872-876.

Faure Walker, J., Boncio, P., Pace, B., Roberts, G., Benedetti, L., Scotti, O., Visini, F. and Peruzza, L., 2021. Fault2SHA Central Apennines database and structuring active fault data for seismic hazard assessment. Scientific data, 8(1), p.87.

Fellin, M.G., San Jose, M., Faccenna, C., Willett, S.D., Cosentino, D., Lanari, R., Gourbet, L. and Maden, C., 2022. Transition from slab roll-back to slab break-off in the central Apennines, Italy: Constraints from the stratigraphic and thermochronologic record. GSA Bulletin, 134(7-8), pp.1916-1930.

Ferré, E.C., Chou, Y.M., Kuo, R.L., Yeh, E.C., Leibovitz, N.R., Meado, A.L., Campbell, L. and Geissman, J.W., 2016. Deciphering viscous flow of frictional melts with the mini-AMS method. *Journal of Structural Geology*, *90*, pp.15-26.

Fondriest, M., Smith, S.A., Candela, T., Nielsen, S.B., Mair, K. and Di Toro, G., 2013. Mirror-like faults and power dissipation during earthquakes. *Geology*, *41*(11), pp.1175-1178.

Fondriest, M., Aretusini, S., Di Toro, G. and Smith, S.A., 2015. Fracturing and rock pulverization along an exhumed seismogenic fault zone in dolostones: The Foiana Fault Zone (Southern Alps, Italy). *Tectonophysics*, 654, pp.56-74.

Galadini, F. and Galli, P., 1999. The Holocene paleoearthquakes on the 1915 Avezzano earthquake faults (central Italy): implications for active tectonics in the central Apennines. *Tectonophysics*, *308*(1-2), pp.143-170.

Gasparini, C., Iannaccone, G. and Scarpa, R., 1985. Fault-plane solutions and seismicity of the Italian peninsula. *Tectonophysics*, *117*(1-2), pp.59-78.

Galadini, F.A. and Messina, P.A., 2001. Plio-Quaternary tectonics of the Fucino basin and surrounding areas (central Italy). *Giornale di Geologia*, 56(2), pp.73-99.

Ghisetti, F. and Vezzani, L., 1999. Depth and modes of Pliocene–Pleistocene crustal extension of the Apennines (Italy). *Terra Nova*, *11*(2-3), pp.67-72.

Gialanella, S., Girardi, F., Ischia, G., Lonardelli, I., Mattarelli, M. & Montagna, M. On the goethite to hematite phase transformation. J. Therm. Anal. Calorim. 102, 867–873 (2010).

Gunatilake, T. and Miller, S.A., 2022. Spatio-temporal complexity of aftershocks in the Apennines controlled by permeability dynamics and decarbonization. *Journal of Geophysical Research: Solid Earth*, 127(6), p.e2022JB024154.

Han, R., Hirose, T. and Shimamoto, T., 2010. Strong velocity weakening and powder lubrication of simulated carbonate faults at seismic slip rates. *Journal of Geophysical Research: Solid Earth*, 115(B3).

Han, R., Shimamoto, T., Hirose, T., Ree, J.H. and Ando, J.I., 2007. Ultralow friction of carbonate faults caused by thermal decomposition. *Science*, 316(5826), pp.878-881.

Han, R.S., Liu, C.Q., Huang, Z.L., Chen, J., Ma, D.Y., Lei, L. and Ma, G.S., 2007. Geological features and origin of the Huize carbonate-hosted Zn–Pb–(Ag) district, Yunnan, South China. *Ore Geology Reviews*, *31*(1-4), pp.360-383.

Hirose, T. and Shimamoto, T., 2005. Growth of molten zone as a mechanism of slip weakening of simulated faults in gabbro during frictional melting. Journal of Geophysical Research: Solid Earth, 110(B5).

Hirt, A.M. and Almqvist, B.S., 2012. Unraveling magnetic fabrics. *International Journal of Earth Sciences*, *101*(3), pp.613-624.

Hladil, J., Gersl, M., Strnad, L., Frana, J., Langrova, A. and Spisiak, J., 2006. Stratigraphic variation of complex impurities in platform limestones and possible significance of atmospheric dust: a study with emphasis on gamma-ray spectrometry and magnetic susceptibility outcrop logging (Eifelian-Frasnian, Moravia, Czech Republic). *International Journal of Earth Sciences*, *95*, pp.703-723.

Hrouda, F., 2004. Problems in interpreting AMS parameters in diamagnetic rocks. *Geological Society, London, Special Publications*, *238*(1), pp.49-59.

Humphries, T.D., Møller, K.T., Rickard, W.D., Sofianos, M.V., Liu, S., Buckley, C.E. & Paskevicius, M. 2019. Dolomite: a low-cost thermochemical energy storage material. *Journal of Materials Chemistry*, 7, 1206–1215.

Jelinek, V., 1981. Characterization of the magnetic fabric of rocks. *Tectonophysics*, *79*(3-4), pp.T63-T67.

Issachar, R., Levi, T., Marco, S. and Weinberger, R., 2018. Separation of diamagnetic and paramagnetic fabrics reveals strain directions in carbonate rocks. *Journal of Geophysical Research: Solid Earth*, *123*(3), pp.2035-2048.

Kim, H.N., So, B.D., Kim, M.S., Han, K.S. and Oh, S.B., 2021. Seismic fault weakening via CO2 pressurization enhanced by mechanical deformation of dolomite fault gouges. *Geology*, 49(10), pp.1245-1249.

Kuo, L.W., Song, S.R., Suppe, J. and Yeh, E.C., 2016. Fault mirrors in seismically active fault zones: A fossil of small earthquakes at shallow depths. *Geophysical Research Letters*, *43*(5), pp.1950-1959.

Lavallée, Y., Hirose, T., Kendrick, J.E., Hess, K.U. and Dingwell, D.B., 2015. Fault rheology beyond frictional melting. Proceedings of the National Academy of Sciences, 112(30), pp.9276-9280.

Levi, T., Weinberger, R. and Marco, S., 2014. Magnetic fabrics induced by dynamic faulting reveal damage zone sizes in soft rocks, Dead Sea basin. *Geophysical Journal International*, *199*(2), pp.1214-1229.

Levi, T. and Weinberger, R., 2011. Magnetic fabrics of diamagnetic rocks and the strain field associated with the Dead Sea Fault, northern Israel. *Journal of Structural Geology*, *33*(4), pp.566-578.

Li, H., Wang, H., Xu, Z., Si, J., Pei, J., Li, T., Huang, Y., Song, S.R., Kuo, L.W., Sun, Z. and Chevalier, M.L., 2013. Characteristics of the fault-related rocks, fault zones and the principal slip zone in the Wenchuan Earthquake Fault Scientific Drilling Project Hole-1 (WFSD-1). *Tectonophysics*, 584, pp.23-42.

Lockner, D.A., Morrow, C., Moore, D. and Hickman, S., 2011. Low strength of deep San Andreas fault gouge from SAFOD core. *Nature*, 472(7341), pp.82-85.

Ma, K.F., Tanaka, H., Song, S.R., Wang, C.Y., Hung, J.H., Tsai, Y.B., Mori, J., Song, Y.F., Yeh, E.C., Soh, W. and Sone, H., 2006. Slip zone and energetics of a large earthquake from the Taiwan Chelungpu-fault Drilling Project. *Nature*, *444*(7118), pp.473-476.

Martín-Hernández, F. and Ferré, E.C., 2007. Separation of paramagnetic and ferrimagnetic anisotropies: A review. *Journal of Geophysical Research: Solid Earth*, *112*(B3).

Mattsson, T., Petri, B., Almqvist, B., McCarthy, W., Burchardt, S., Palma, J.O., Hammer, Ø. and Galland, O., 2021. Decrypting magnetic fabrics (AMS, AARM, AIRM) through the analysis of mineral shape fabrics and distribution anisotropy. *Journal of Geophysical Research: Solid Earth*, *126*(6), p.e2021JB021895.

McCabe, C., Jackson, M. and Ellwood, B.B., 1985. Magnetic anisotropy in the Trenton limestone: results of a new technique, anisotropy of anhysteretic susceptibility. *Geophysical Research Letters*, *12*(6), pp.333-336.

Merico, A., Iezzi, G., Pace, B., Ferranti, L., Cremona, M., Scafa, M., Cavallo, A., Colella, A., Nazzari, M. and Scarlato, P., 2020. Grain size and grain size distribution of a lithified fault core in carbonates rocks using multi-scale image analysis: The example of the San Benedetto-Gioia dei Marsi fault (Central Italy). *Journal of Structural Geology*, *134*, p.104017.

Michetti, A.M., Brunamonte, F., Serva, L. and Vittori, E., 1996. Trench investigations of the 1915 Fucino earthquake fault scarps (Abruzzo, Central Italy): geological evidence of large historical events. *Journal of Geophysical Research: Solid Earth*, *101*(B3), pp.5921-5936.

Mizoguchi, K., Hirose, T., Shimamoto, T. and Fukuyama, E., 2007. Reconstruction of seismic faulting by high-velocity friction experiments: An example of the 1995 Kobe earthquake. *Geophysical Research Letters*, *34*(1).

Molina Garza, R.S., Geissman, J., Wawrzyniec, T., Weber, B., Martínez, M.L. and Aranda-Gómez, J., 2009. An integrated magnetic and geological study of cataclasite-dominated pseudotachylytes in the Chiapas Massif, Mexico: a snapshot of stress orientation following slip. *Geophysical Journal International*, *177*(3), pp.891-912.

Moro, M., Saroli, M., Tolomei, C. and Salvi, S., 2009. Insights on the kinematics of deep-seated gravitational slope deformations along the 1915 Avezzano earthquake fault (Central Italy), from time-series DInSAR. *Geomorphology*, *112*(3-4), pp.261-276.

Niemeijer, A., Di Toro, G., Griffith, W.A., Bistacchi, A., Smith, S.A. and Nielsen, S., 2012. Inferring earthquake physics and chemistry using an integrated field and laboratory approach. *Journal of Structural Geology*, *39*, pp.2-36.

Oddone, E., 1915. Gli elementi fisici del grande terremoto marsicano-fucense del 13 gennaio 1915. Le osservazioni macrosismiche. *Bollettino della Società Sismologica Italiana*, 19, pp.71-217.

Ohl, M., Plümper, O., Chatzaras, V., Wallis, D., Vollmer, C. and Drury, M., 2020. Mechanisms of fault mirror formation and fault healing in carbonate rocks. *Earth and Planetary Science Letters*, 530, p.115886.

Palyvos, N., Pantosti, D., De Martini, P.M., Lemeille, F., Sorel, D. and Pavlopoulos, K., 2005. The Aigion–Neos Erineos coastal normal fault system (western Corinth Gulf Rift, Greece): Geomorphological signature, recent earthquake history, and evolution. *Journal of Geophysical Research: Solid Earth*, 110(B9).

Parés, J.M., 2015. Sixty years of anisotropy of magnetic susceptibility in deformed sedimentary rocks. *Frontiers in Earth Science*, *3*, p.4.

Passelègue, F.X., Aubry, J., Nicolas, A., Fondriest, M., Deldicque, D., Schubnel, A. and Di Toro, G., 2019. From fault creep to slow and fast earthquakes in carbonates. *Geology*, *47*(8), pp.744-748.

Piccardi, L., Gaudemer, Y., Tapponnier, P. and Boccaletti, M., 1999. Active oblique extension in the central Apennines (Italy): evidence from the Fucino region. Geophysical Journal International, 139(2), pp.499-530.

Ponomar, V.P. Thermomagnetic properties of the goethite transformation during high-temperature treatment. Miner. Eng. 127, 143–152 (2018).

Pozzi, G., De Paola, N., Nielsen, S.B., Holdsworth, R.E. and Bowen, L., 2018. A new interpretation for the nature and significance of mirror-like surfaces in experimental carbonate-hosted seismic faults. *Geology*, *46*(7), pp.583-586.

Ren, C., Wang, Z., Taymaz, T., Hu, N., Luo, H., Zhao, Z., Yue, H., Song, X., Shen, Z., Xu, H. and Geng, J., 2024. Supershear triggering and cascading fault ruptures of the 2023 Kahramanmaraş, Türkiye, earthquake doublet. *Science*, *383*(6680), pp.305-311.

Renard, F. and Candela, T., 2017. Scaling of fault roughness and implications for earthquake mechanics. *Fault zone dynamic processes: Evolution of fault properties during seismic rupture*, pp.195-215.

Rice, J.R., 2017. Heating, weakening and shear localization in earthquake rupture. *Philosophical Transactions of the Royal Society A: Mathematical, Physical and Engineering Sciences*, *375*(2103), p.20160015.

Roberts, A.P., Florindo, F., Chang, L., Heslop, D., Jovane, L. and Larrasoaña, J.C., 2013. Magnetic properties of pelagic marine carbonates. *Earth-science reviews*, *127*, pp.111-139.

Robinson, E.V. (1915). A Visit to the Avezzano Eaethquake Zone, Journal of Geography, 13:9, 265-269, DOI: 10.1080/00221341508983666.

Rowe, C.D., Fagereng, Å., Miller, J.A. and Mapani, B. 2012. Signature of coseismic decarbonation in dolomitic fault rocks of the Naukluft Thrust, Namibia. *Earth and Planetary Science Letters*, 333: 200-210.

Sagy, A. and Brodsky, E.E., 2009. Geometric and rheological asperities in an exposed fault zone. *Journal of Geophysical Research: Solid Earth*, *114*(B2).

Schmidt, V., Hirt, A.M., Rosselli, P. and Martín-Hernández, F., 2007. Separation of diamagnetic and paramagnetic anisotropy by high-field, low-temperature torque measurements. *Geophysical Journal International*, *168*(1), pp.40-47.

Schmidt, V., Günther, D. and Hirt, A.M., 2006. Magnetic anisotropy of calcite at room-temperature. *Tectonophysics*, *418*(1-2), pp.63-73.

Scisciani, V., 2009. Styles of positive inversion tectonics in the Central Apennines and in the Adriatic foreland: Implications for the evolution of the Apennine chain (Italy). *Journal of Structural Geology*, *31*(11), pp.1276-1294.

Serva, L., Blumetti, A.M., Guerrieri, L.U.C.A. and Michetti, A.M., 2002. The Apennine intermountain basins: the result of repeated strong earthquakes over a geological time interval. *Boll. Soc. Geol. It*, *1*, pp.939-946.

Serva, L., 1986. Gli effetti sul terreno del terremoto del Fucino (13-1-1915); tentativo di interpretazione della evoluzione tettonica recente di alcune strutture. In *Geologia dell'Italia centrale. Congresso nazionale. 73*, pp. 387-390.

Sgobba, S.A. and Pacor, F., 2023. An application of the NonErgodic ground ShaKing (NESK) approach to an historical earthquake scenario: The case-study of the 1915 Fucino earthquake (central Italy). *Soil Dynamics and Earthquake Engineering*, *164*, p.107622.

Sibson, R.H., 1975. Generation of pseudotachylyte by ancient seismic faulting. *Geophysical Journal International*, *43*(3), pp.775-794.

Sibson, R.H., Toy, V.G. and Abercrombie, R., 2006. The habitat of fault-generated pseudotachylyte: Presence vs. absence of friction-melt. *Geophysical Monograph-American Geophysical Union*, *170*, p.153.

Siman-Tov, S., Aharonov, E., Boneh, Y. and Reches, Z.E., 2015. Fault mirrors along carbonate faults: Formation and destruction during shear experiments. *Earth and Planetary Science Letters*, *430*, pp.367-376.

Siman-Tov, S., Aharonov, E., Sagy, A. and Emmanuel, S., 2013. Nanograins form carbonate fault mirrors. *Geology*, *41*(6), pp.703-706.

Smeraglia, L., Bettucci, A., Billi, A., Carminati, E., Cavallo, A., Di Toro, G., Natali, M., Passeri, D., Rossi, M. and Spagnuolo, E., 2017. Microstructural evidence for seismic and aseismic slips along clay-bearing, carbonate faults. *Journal of Geophysical Research: Solid Earth*, *122*(5), pp.3895-3915.

Smeraglia, L., Fabbi, S., Cipriani, A., Consorti, L., Sirna, M., Corbi, F., Pizzati, M., Parotto, M. and Cavinato, G.P., 2024. Deformation mechanisms and slip behaviors of tectonically deformed conglomerates from the Central Apennines fold-and-thrust belt: Implications for shallow aseismic and seismic slip. *Journal of Structural Geology*, *186*, p.105202.

Smith, S.A., Billi, A., Toro, G.D. and Spiess, R., 2011. Principal slip zones in limestone: microstructural characterization and implications for the seismic cycle (Tre Monti Fault, Central Apennines, Italy). *Pure and Applied Geophysics*, *168*, pp.2365-2393.

Spray, J.G., 2010. Frictional melting processes in planetary materials: From hypervelocity impact to earthquakes. *Annual Review of Earth and Planetary Sciences*, *38*(1), pp.221-254.

Storti, F., Holdsworth, R.E. and Salvini, F., 2003. Intraplate strike-slip deformation belts. *Geological Society, London, Special Publications*, *210*(1), pp.1-14.

Sulem, J. and Famin, V., 2009. Thermal decomposition of carbonates in fault zones: Slip-weakening and temperature-limiting effects. *Journal of Geophysical Research: Solid Earth*, *114*(B3).

Sutherland, R., Toy, V.G., Townend, J., Cox, S.C., Eccles, J.D., Faulkner, D.R., Prior, D.J., Norris, R.J., Mariani, E., Boulton, C. and Carpenter, B.M., 2012. Drilling reveals fluid control on architecture and rupture of the Alpine fault, New Zealand. *Geology*, *40*(12), pp.1143-1146.

Tarling, D. and Hrouda, F. eds., 1993. *Magnetic anisotropy of rocks*. Springer Science & Business Media.

Tortorici, Giuseppe, Gino Romagnoli, Sabrina Grassi, Sebastiano Imposa, Giuseppe Lombardo, Francesco Panzera, and Stefano Catalano. "Quaternary negative tectonic inversion along the Sibillini Mts. thrust zone: the Arquata del Tronto case history (Central Italy)." *Environmental Earth Sciences* 78, no. 1 (2019): 37.

Vezzani, L., Festa, A. and Ghisetti, F.C., 2010. *Geology and tectonic evolution of the Central-Southern Apennines, Italy* (Vol. 469). Geological Society of America.

Villani, F., Tulliani, V., Sapia, V., Fierro, E., Civico, R. and Pantosti, D., 2015. Shallow subsurface imaging of the Piano di Pezza active normal fault (central Italy) by high-resolution refraction and electrical resistivity tomography coupled with time-domain electromagnetic data. *Geophysical Supplements to the Monthly Notices of the Royal Astronomical Society*, *203*(3), pp.1482-1494.

Violay, M., Nielsen, S., Spagnuolo, E., Cinti, D., Di Toro, G. and Di Stefano, G., 2013. Pore fluid in experimental calcite-bearing faults: Abrupt weakening and geochemical signature of co-seismic processes. *Earth and planetary science letters*, *361*, pp.74-84.

Volatili, T., Agosta, F., Cardozo, N., Zambrano, M., Lecomte, I. and Tondi, E., 2022. Outcrop-scale fracture analysis and seismic modelling of a basin-bounding normal fault in platform carbonates, central Italy. *Journal of Structural Geology*, *155*, p.104515.

Walter, D., Buxbaum, G. & Laqua, W. The mechanism of the thermal transformation from goethite to hematite. J. Therm. Anal. Calorim. 63, 733–748 (2001).

Ward, S.N. and Valensise, G.R., 1989. Fault parameters and slip distribution of the 1915 Avezzano, Italy, earthquake derived from geodetic observations. *Bulletin of the Seismological Society of America*, *79*(3), pp.690-710.

Wells, D.L. and Coppersmith, K.J., 1994. New empirical relationships among magnitude, rupture length, rupture width, rupture area, and surface displacement. *Bulletin of the seismological Society of America*, *84*(4), pp.974-1002.

Yang, T., Chou, Y.M., Ferré, E.C., Dekkers, M.J., Chen, J., Yeh, E.C. and Tanikawa, W., 2020. Faulting processes unveiled by magnetic properties of fault rocks. *Reviews of Geophysics*, *58*(4), p.e2019RG000690.

Zamanialavijeh, N., Hosseinzadehsabeti, E., Ferré, E.C., Hacker, D.B., Biedermann, A.R. and Biek, R.F., 2021. Kinematics of frictional melts at the base of the world's largest terrestrial landslide: Markagunt gravity slide, southwest Utah, United States. *Journal of structural geology*, *153*, p.104448.

Zamani, N., Heij, G.W., Ferré, E.C., Murphy, M.A. and Bagley, B., 2023. High-Velocity Slip and Thermal Decomposition of Carbonates: Example From the Heart Mountain Slide Ultracataclasites, Wyoming. *Journal of Geophysical Research: Solid Earth*, *128*(5), p.e2022JB026185.

Zamani, N., Murphy, M.A., Ferré, E.C., and Barou, F. (2025). Unraveling carbonate fault dynamics, from friction to decarbonation, through the 1959 Mw 7.2 earthquake in Montana. *Scientific Reports*, 10.1038/s41598-025-89071-4.

Zhang, L., Li, H., Ferré, E.C., Sun, Z., Chou, Y.M., Cao, Y., Wang, H., Zheng, Y., Li, C. and Hosseinzadehsabeti, E., 2024. Focal mechanism of a Late Triassic large magnitude earthquake along the Longmen Shan fault belt, eastern Tibetan Plateau. *Journal of Structural Geology*, *178*, p.105015.

Table 2. Magnetic hysteresis parameters of the Venere Fault rocks (mirror)

Sample #	mass	M_s	M_s	M_r	M_r	H_c	H_{cr}	M_r/M_s	H_{cr}/H_c	Mag*
	g	10^{-6} Am^2	10^{-6} Am^2/kg	10^{-6} Am^2	10^{-6} Am^2/kg	*mT*	*mT*			*ppm*
VEN04_467	0.467	0.187	400	0.0148	32	7.0	30.5	0.079	4.38	0.230
VEN06_177	0.177	0.167	945	0.0268	151	9.7	26.5	0.160	2.73	0.097
VEN06_350	0.350	0.024	68	0.0039	11	12.1	26.2	0.163	2.17	1.361
VEN06_440	0.440	0.172	390	0.0217	49	8.1	27.4	0.126	3.39	0.236
VEN06_540	0.540	0.071	131	0.0061	11	8.0	27.4	0.087	3.41	0.702
VEN06_932	0.942	0.200	213	0.0332	35	7.2	25.9	0.166	3.61	0.433
VEN06_1292	1.292	0.226	175	0.0287	22	10.5	24.3	0.127	2.31	0.527
VEN07_347	0.347	0.186	535	0.0120	35	6.7	27.8	0.065	4.17	0.172
VEN07_550	0.550	0.079	143	0.0101	18	6.2	25.9	0.128	4.16	0.642
min.	**0.177**	**0.024**	**68**	**0.0039**	**11.0**	**6.22**	**24.3**	**0.065**	**2.174**	**0.097**
max.	**1.292**	**0.226**	**945**	**0.0332**	**151.3**	**12.06**	**30.5**	**0.166**	**4.382**	**1.361**
average	**0.567**	**0.146**	**333**	**0.0175**	**40.6**	**8.38**	**26.9**	**0.122**	**3.371**	**0.489**
median	**0.467**	**0.172**	**213**	**0.0148**	**31.6**	**8.05**	**26.5**	**0.127**	**3.410**	**0.433**
2σ errors	**0.719**	**0.142**	**574**	**0.0205**	**92.6**	**5.22**	**14.0**	**0.084**	**2.059**	**0.811**

Notes: H_c - magnetic coercitive force, M_r - magnetic remanence after saturation, M_s - saturation magnetization, H_{cr} - coercivity of magnetic remanence, Mag* - concentration of magnetite in parts per million calculated assuming that magnetite has a saturation magnetization of 92 Am^2/kg.

Table 3. Anisotropy of anhysteretic remanent magnetization (AARM) of the Venere Fault mirror (VEN06)

	Sample #	*mass*	*Ji*	*P'*	*T*	*J1d*	*J1i*	*J2d*	*J2i*	*J3d*	*J3i*
		g	10^{-6} Am^2			°	°	°	°	°	°
VEN04	VEN04S1C02	0.120	0.732	1.05	-0.059	257	11	164	16	22	70
	VEN04S1C04	0.116	0.630	1.06	0.206	15	18	264	48	119	36
	VEN04S1C05	0.116	0.743	1.08	0.599	145	13	247	41	40	46
	VEN04S1C06	0.115	0.510	1.15	-0.039	237	47	330	3	62	43
	VEN04S1C10	0.103	0.619	1.10	0.402	90	6	184	31	350	58
	VEN04S1C14	0.100	0.511	1.11	-0.501	130	19	13	53	231	30
	VEN04S1C15	0.105	0.526	1.36	-0.672	199	48	104	4	11	41
	VEN04S1C17	0.104	0.824	1.08	-0.385	117	4	26	13	224	76
	VEN04S1C19	0.101	0.692	1.09	0.086	170	39	289	30	44	36
	VEN04S1C20	0.100	0.773	1.06	0.353	282	20	162	53	24	29
	VEN04S1C21	0.118	0.762	1.30	-0.537	330	86	86	2	176	3
	max.	*0.120*	*0.824*	*1.362*	*0.599*						
	min.	*0.100*	*0.510*	*1.054*	*-0.672*						
	average	*0.108*	*0.656*	*1.117*	*-0.001*						
	stdev.	*0.008*	*0.114*	*0.091*	*0.415*						
VEN06	VEN06S1C01	0.140	1.07	1.07	0.565	318	4	226	27	55	62
	VEN06S1C02	0.120	3.67	1.03	0.273	118	9	215	37	17	51
	VEN06S1C03	0.123	0.70	1.29	0.194	290	54	145	31	45	17
	VEN06S1C04	0.125	0.81	1.08	-0.520	122	8	213	12	357	76
	VEN06S1C05	0.131	0.82	1.07	-0.212	110	10	201	6	322	78
	VEN06S1C07	0.131	0.81	1.09	0.001	132	13	223	8	344	75
	VEN06S1C08	0.125	0.91	1.11	-0.161	118	12	217	35	12	52
	VEN06S1C10	0.114	2.55	1.06	0.315	130	56	246	16	345	29
	VEN06S1C12	0.115	0.74	1.03	0.007	243	5	141	66	335	24
	VEN06S1C13	0.130	0.78	1.22	-0.768	174	36	282	23	37	46
	VEN06S1C14	0.116	0.85	1.56	0.685	241	28	149	4	52	62
	VEN06S1C15	0.122	0.69	1.10	0.362	322	4	229	35	58	54
	VEN06S1C19	0.125	0.74	1.07	0.660	315	10	214	51	53	38
	VEN06S1C20	0.130	0.77	1.04	0.087	317	7	217	55	52	34
	VEN06S1C23	0.125	1.40	1.08	-0.015	178	42	292	24	43	38
	VEN06S1C24	0.121	4.98	1.09	0.380	194	62	35	27	301	9
	VEN06S1C25	0.114	0.71	1.08	0.518	321	6	223	51	55	39
	VEN06S1C27	0.130	0.80	1.11	0.392	193	29	296	22	57	52
	VEN06S1C28	0.130	1.45	1.12	0.009	180	47	287	15	30	39
	VEN06S1C29	0.114	2.87	1.09	-0.495	163	67	54	8	321	22
	min.	*0.114*	*0.689*	*1.030*	*-0.768*						
	max.	*0.140*	*4.981*	*1.559*	*0.685*						
	average	*0.124*	*1.406*	*1.142*	*0.062*						
	stdev.	*0.007*	*1.184*	*0.152*	*0.428*						

Table 1. Composition and bulk magnetic susceptibility of the Venere Fault rocks

XRD - fault mirror cataclasite: calcite V_{cal} ~ 99.99%, 0.01% other
limestone density - ρ = 2710 kg/m^3

	Magnetic susceptibility K_m 10^{-6} [SI]	χ_m 10^{-9} . $m^3 \cdot kg^{-1}$
pure calcite (Schmidt et al., 2006) (K_{cal})	*-12.09*	*-4.46*
VEN02 fault core	-6.29	-2.32
VEN03 fault core	-1.22	-0.45
VEN04 fault mirror (top 3.5 mm)	7.95	2.93
VEN06 fault mirror (top 3.5 mm)	2.30	0.85
VEN07 fault core	5.22	1.93
VEN08 fault core	-7.57	-2.79
VEN09 fault core	-3.54	-1.31
VEN10 fault core	-7.15	-2.64
VEN12 fault core	-1.81	-0.67
VEN13 fault core	-7.88	-2.91
VEN14 fault core	-2.26	-0.83
VEN average undeformed limestone (10 samples)	-3.01	-1.11
VEN average fault core (9 samples)	-3.61	-1.33
VEN average fault mirror (2 samples)	5.13	1.89

$K_m = K_{dia} + K_{para} + K_{ferro}$ (Equation 1)

K_{dia} - diamagnetic susceptibility, $K_{dia} = K_{cal} \times V_{cal}$ (Siegesmund et al., 1995)	-12.09	-4.46
K_{para} - paramagnetic susceptibility, from hysteresis high-field slope	0.456	0.17
K_{ferro} - ferromagnetic susceptibility (from Eq. 1) - undeformed limestone	8.62	3.18
K_{ferro} - ferromagnetic susceptibility (from Eq. 1) - fault core	8.02	2.96
K_{ferro} - ferromagnetic susceptibility (from Eq. 1) - fault mirror	16.75	6.18

Table 4. Parameters, units, and equations of frictional heat on the Venere Fault plane

Parameters (symbols)	*Units*	Frictional heat
normal stress (σ_n)	kPa	13.12
shear stress (σ_s)	kPa	12.23
fault dip angle (θ)*	o	43
rock density (p)	kg/m^3	2500
gravity (g)	m/s^2	9.81
depth (d)	m	1
lithostatic stress (a)	Pa	2.45E+04
lithostatic stress (a)	kPa	24.53
frictional heat produced (Q_f)	J	1.22E+04
heat-transfer-distance (D) after 10 s[#]	mm	3.38
thermal diffusivity (κ)	mm^{2}s^{-1}	1.14
time in seconds (t)	s	10
enthalpy of the reaction (ΔH)[1]	J/mol	1.87E+05
specific heat (Cp)[2]	J/kg.°C	8.54E+02
temperature difference (ΔT)	ºC	525
molecular weight of dolomite (m_d)	kg	0.1844
energy released during faulting (W_f)	J	
radiated seismic energy (E)	J	
seismic slip (d)	m	
thermal energy for decarbonation (Q_d)	J	
total mass of rock (m)	kg	

Equations for 43º dip angle		
$W_f = Q_f + E$ [Equation (1)[4]]		
$W_f \approx Q_f$ [Equation (2)[4]]		
$W_f \approx d \cdot \sigma_s$ [Equation (3)[3]]		
$Q_f \approx d \cdot \sigma_s$ [Equation (4)]	1.22E+04	J
$D = (\kappa t)^{0.5}$ [Equation (5)[3]]	3.38	mm
$Q_d = C_p\Delta T + \Delta H$ [Equation (6)]	1.46E+06	J
decarbonated mass over 1 m^2	0.004	kg
thickness of decarbonated rock	1.7	µm

Sources

[1]Criado et al. (1995)

[2]Stout and Robie (1963)

[3]Andersen and Austrheim (2006)

[4]Scholtz (2019)

*field measurements on Venere Fault

#estimated duration of 1915 seismic slip

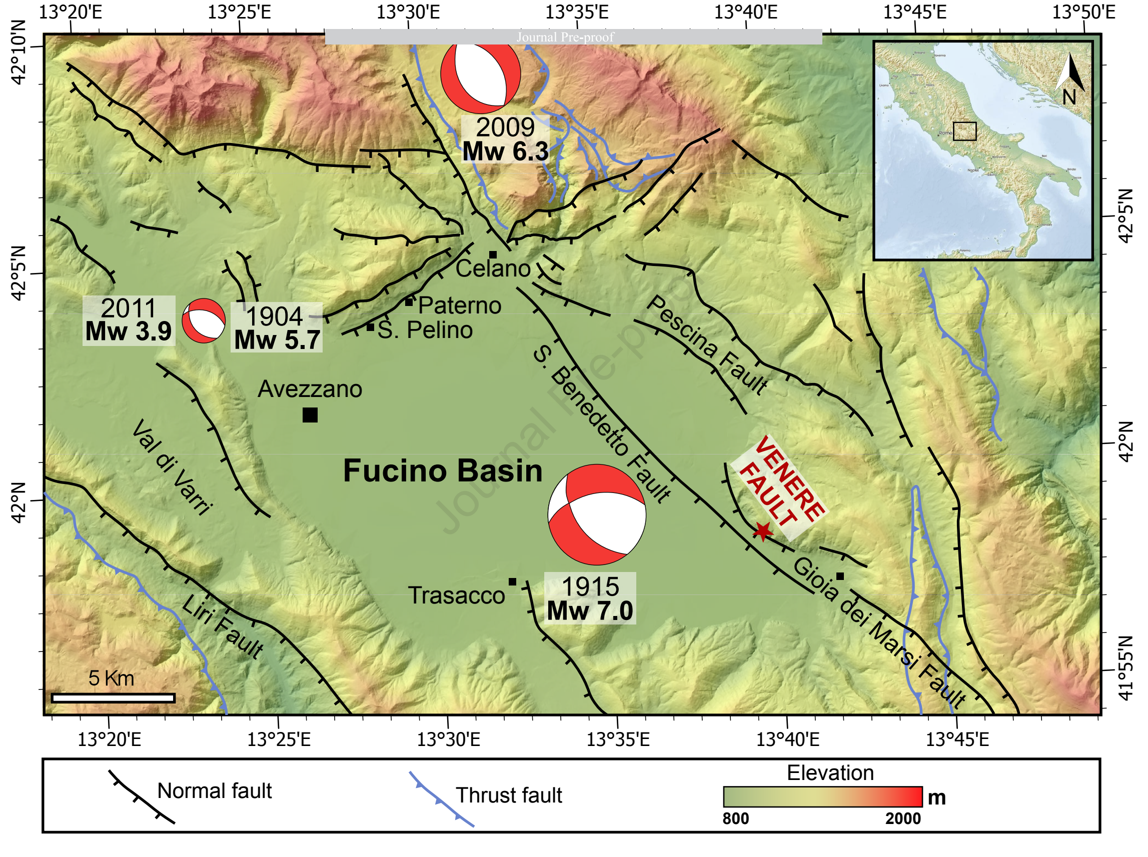

13°20'E
13°25'E
13°30'E
13°35'E
13°40'E
13°45'E
13°50'E
42°10'N
42°5'N
42°N
41°55'N
2009
Mw 6.3
2011
Mw 3.9
1904
Mw 5.7
Celano
Paterno
S. Pelino
Avezzano
Pescina Fault
S. Benedetto Fault
Val di Varri
Fucino Basin
VENERE FAULT
1915
Mw 7.0
Trasacco
Gioia dei Marsi Fault
Liri Fault
5 Km
N
Normal fault
Thrust fault
Elevation
m
800
2000

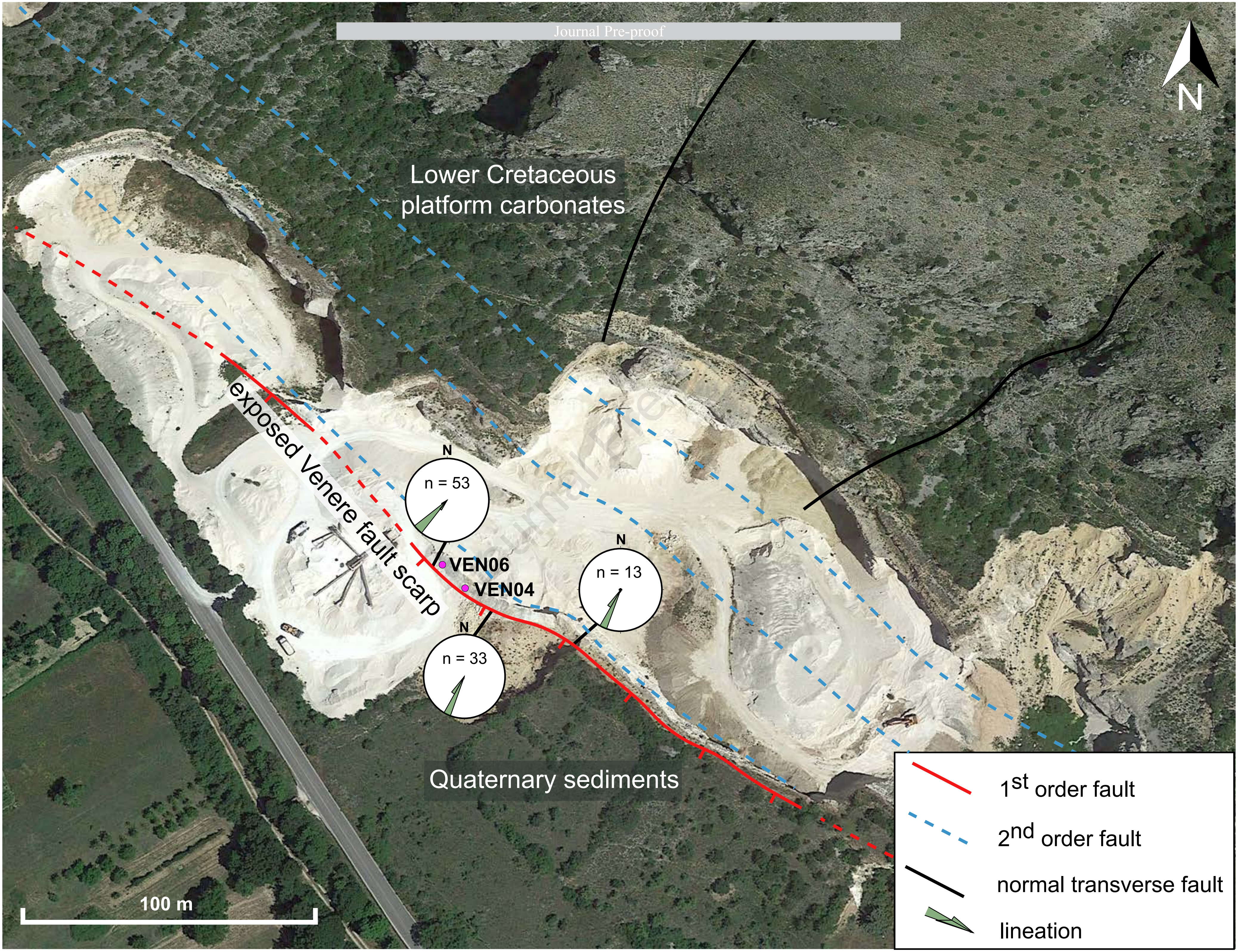
Lower Cretaceous
platform carbonates
exposed Venere fault scarp
N
n = 53
VEN06
VEN04
N
n = 13
N
n = 33
Quaternary sediments
100 m
1st order fault
2nd order fault
normal transverse fault
lineation

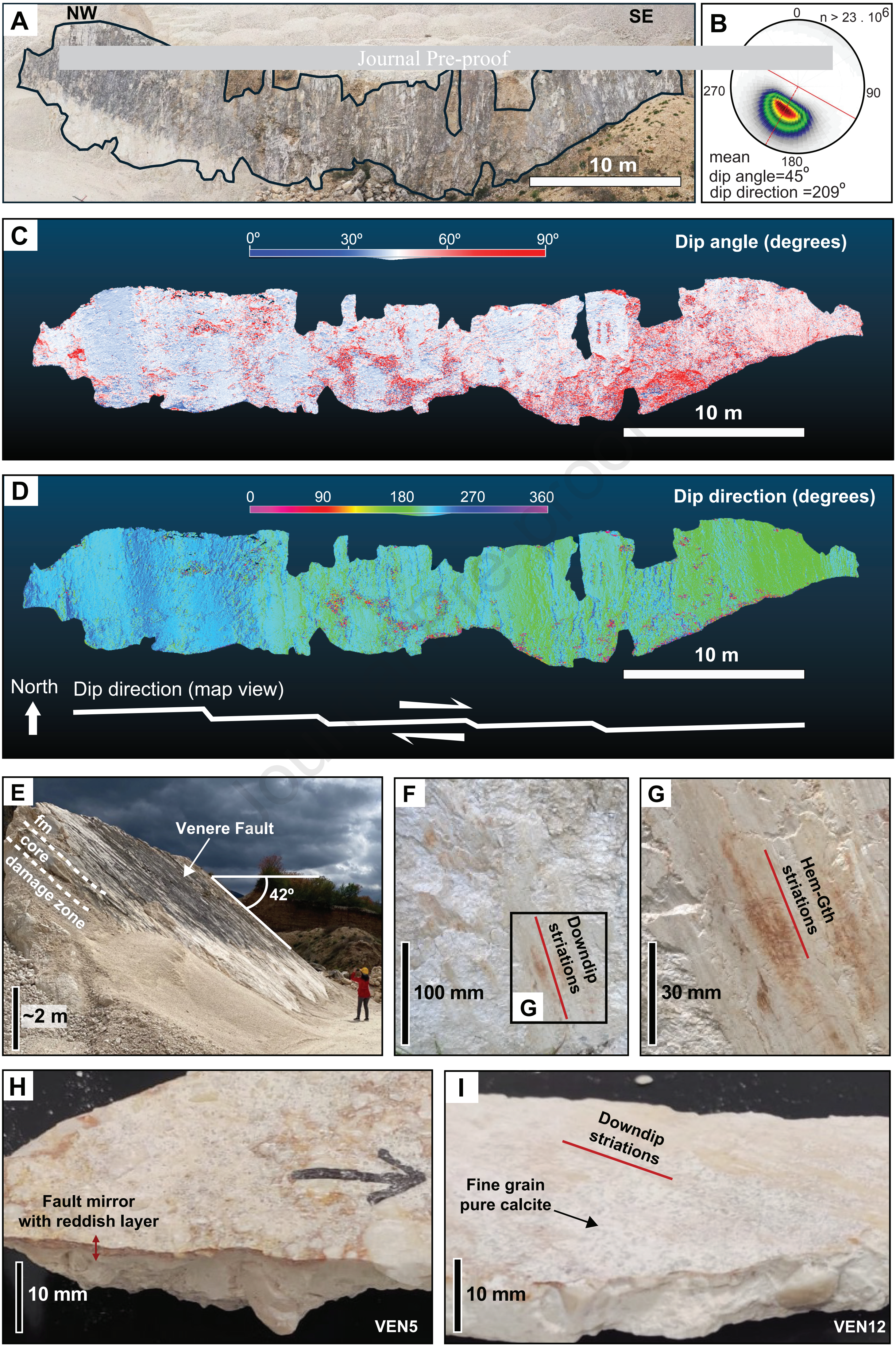
A
NW
SE
Journal Pre-proof
10 m
B
n > 23 . 10^6
0
90
180
270
mean
dip angle=45°
dip direction =209°
C
0°
30°
60°
90°
Dip angle (degrees)
10 m
D
0
90
180
270
360
Dip direction (degrees)
10 m
North
Dip direction (map view)
E
fm
core
damage zone
Venere Fault
42°
~2 m
F
Downdip striations
G
100 mm
G
Hem-Gth striations
30 mm
H
Fault mirror with reddish layer
10 mm
VEN5
I
Downdip striations
Fine grain pure calcite
10 mm
VEN12

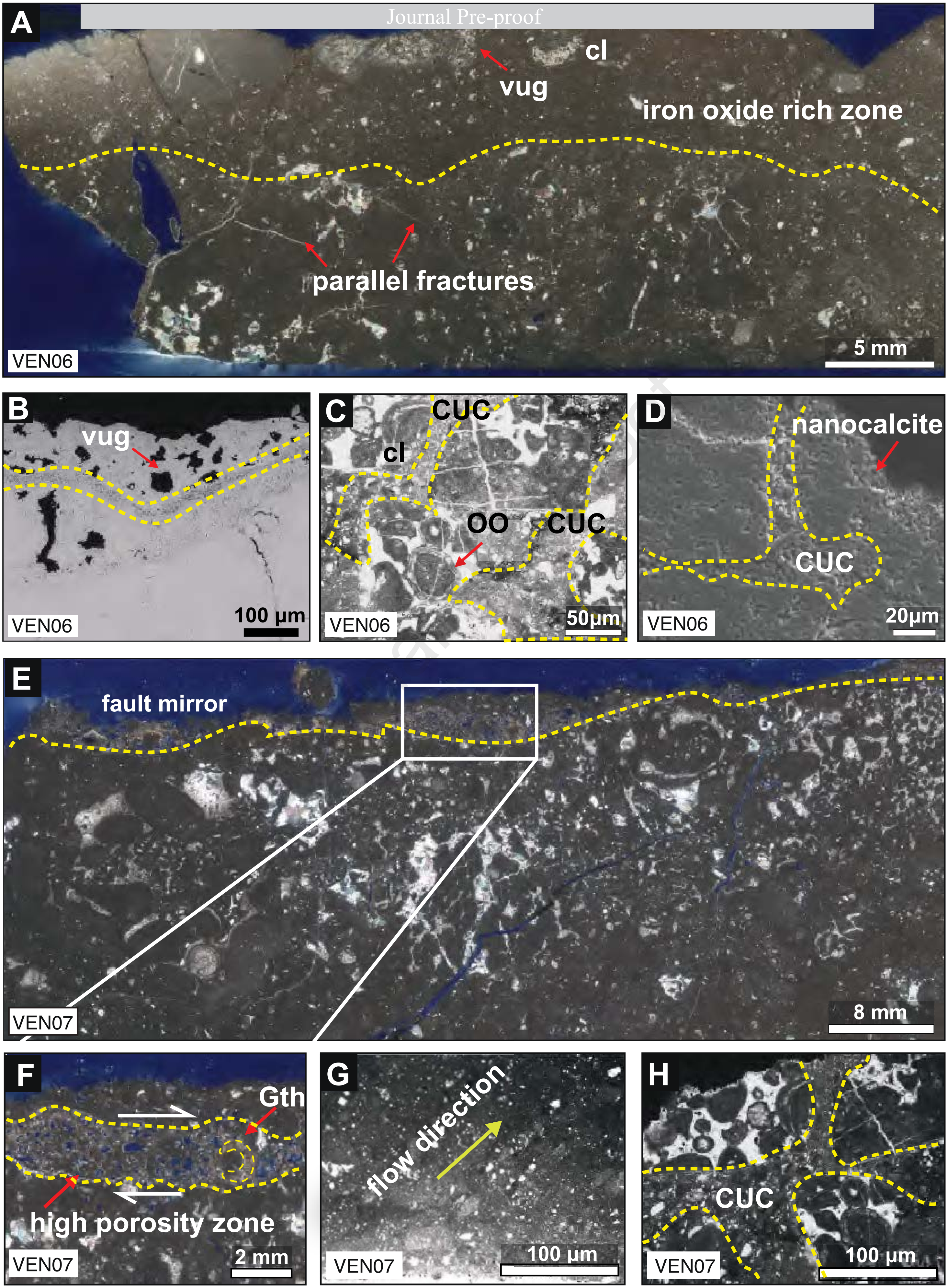
A
cl
vug
iron oxide rich zone
parallel fractures
VEN06
5 mm
B
vug
VEN06
100 μm
C
CUC
cl
OO
CUC
VEN06
50μm
D
nanocalcite
CUC
VEN06
20μm
E
fault mirror
VEN07
8 mm
F
Gth
high porosity zone
VEN07
2 mm
G
flow direction
VEN07
100 μm
H
CUC
VEN07
100 μm

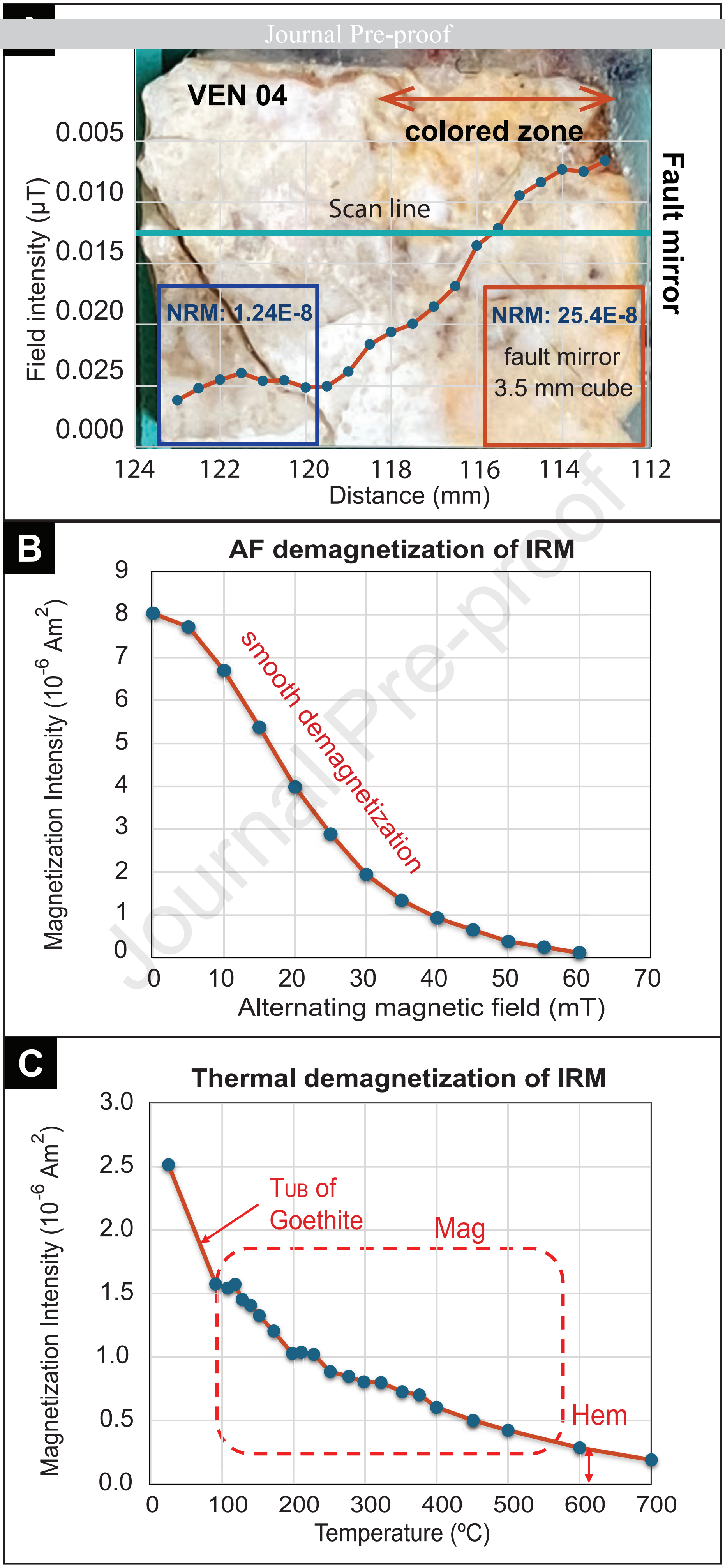

A
VEN 04
colored zone
Fault mirror
Scan line
NRM: 1.24E-8
NRM: 25.4E-8
fault mirror
3.5 mm cube
Field intensity (μT)
0.005
0.010
0.015
0.020
0.025
0.000
124
122
120
118
116
114
112
Distance (mm)
B
AF demagnetization of IRM
smooth demagnetization
Magnetization Intensity (10^{-6} Am^2)
Alternating magnetic field (mT)
C
Thermal demagnetization of IRM
TUB of
Goethite
Mag
Hem
Magnetization Intensity (10^{-6} Am^2)
Temperature (ºC)

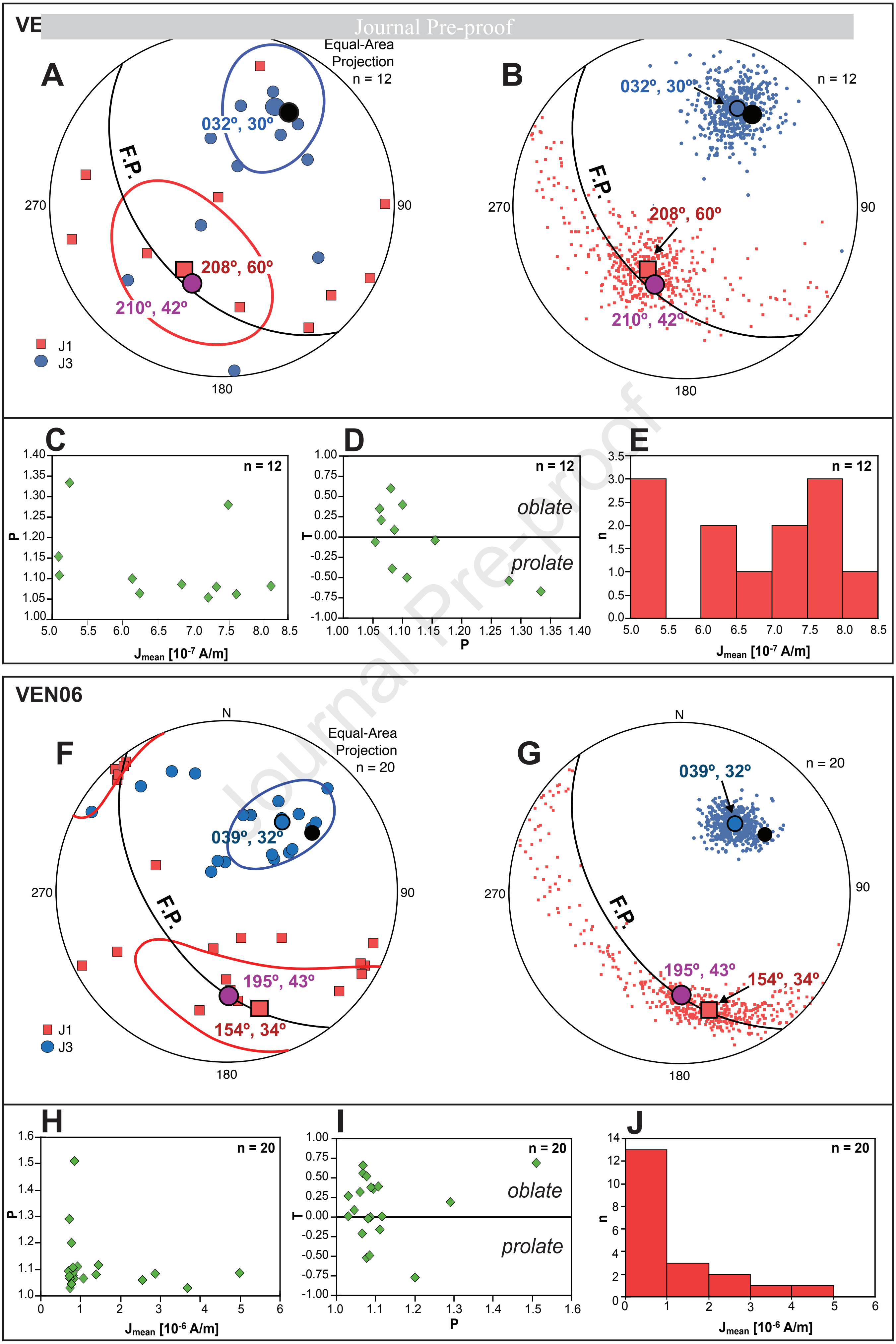
VE
A
Equal-Area
Projection
n = 12
032º, 30º
F.P.
270
90
208º, 60º
210º, 42º
J1
J3
180
B
032º, 30º
n = 12
F.P.
270
90
208º, 60º
210º, 42º
180
C
n = 12
P
Jmean [10-7 A/m]
D
n = 12
oblate
prolate
T
P
E
n = 12
n
Jmean [10-7 A/m]
VEN06
N
F
Equal-Area
Projection
n = 20
039º, 32º
270
90
F.P.
195º, 43º
154º, 34º
J1
J3
180
G
N
039º, 32º
n = 20
270
90
F.P.
195º, 43º
154º, 34º
180
H
n = 20
P
Jmean [10-6 A/m]
I
n = 20
oblate
prolate
T
P
J
n = 20
n
Jmean [10-6 A/m]

Declaration of interests

☒ The authors declare that they have no known competing financial interests or personal relationships that could have appeared to influence the work reported in this paper.

☐ The authors declare the following financial interests/personal relationships which may be considered as potential competing interests: